Serum mitochondrial bioenergetics as fingerprint of the hepatic one: how to monitor genetic MASLD

Running title:

Serum mt-biomarkers to diagnose MASLD

Erika Paolini[1], Miriam Longo[1], Marica Meroni[1], Paola Podini[2], Marco Maggioni[3], Angelo Quattrini[2], Anna Ludovica Fracanzani[1,4], Paola Dongiovanni[1]

[1]Medicine and Metabolic Diseases, Fondazione IRCCS Cà Granda, Ospedale Maggiore Policlinico. Milan, Italy
[2]IRCCS San Raffaele Scientific Institute, Neuropathology Unit, Institute of Experimental Neurology, 20132, Milan, Italy
[3]Division of Pathology, Fondazione IRCCS Ca' Granda Ospedale Maggiore Policlinico, Milan, Italy
[4]Department of Pathophysiology and Transplantation, University of Milan, Milan, Italy.

Correspondence address:
Paola Dongiovanni, MSc
Medicine and Metabolic Diseases; Fondazione IRCCS Cà Granda Ospedale Maggiore Policlinico, Milan, Italy, via Pace 9, 20122 Milano (MI), Italy
Tel: 0039-02-55033467, Fax: 0039-02-55034229; Email: paola.dongiovanni@policlinico.mi.it

Abstract

Metabolic Dysfunction-Associated Steatotic Liver Disease (MASLD) has been an increasing worldwide charge on healthcare owing to scant management and prevention. MASLD pathogenesis is fashioned by environmental and genetic factors and featured by the loss of mitochondrial dynamics. Recently, we demonstrated that the co-presence of loss-of-function polymorphisms in patatin-like phospholipase domain-containing 3 (*PNPLA3*), transmembrane 6 superfamily member 2 (*TM6SF2*) and membrane bound o-acyltransferase domain-containing 7 (*MBOAT7*) hugely predisposed to MASLD progression, revealing first their involvement in mitochondrial maladaptation in a genetics-based knock-out *in vitro* model. To deepen the genetics-mitochondria duo, in this work we generated wild type overexpressed cell lines in which TM6SF2 and/or MBOAT7 deleted proteins were functionally restored, resulting in physiological *spaghetti*-shaped mitochondria characterized by improved OXPHOS capacity. To translate our *in vitro* findings into a clinical perspective, we compared hepatic and peripheral bioenergetic profiles in MASLD patients carrying *PNPLA3*, *MBOAT7* and/or *TM6SF2* variations. The serum mitochondrial respirometry lowered mainly in 3 at-risk variants carriers completely reflecting the hepatic one, thus recommending the applicability of mitochondrial circulating non-invasive biomarkers to prognose genetic MASLD severity.

Introduction

Over the past two decades, Metabolic Dysfunction-Associated Steatotic Liver Disease (MASLD) has depicted a growing burden on health care worldwide, affecting both children and adults [1, 2]. MASLD covers a wide spectrum of chronic liver disorders, ranging from simple steatosis to metabolic dysfunction-associated steatohepatitis (MASH) and fibrosis. In 10–20% of cases, MASH can progress up to cirrhosis and hepatocellular carcinoma (HCC),

and nowadays, it represents the third leading cause of liver transplantation (LT) [3-5]. MASLD is a complex disease whose pathogenesis is shaped by both environmental and genetic factors. Its epidemiology is closely interconnected with epidemic obesity and type 2 diabetes mellitus (T2DM), and it is related to the metabolic syndrome (MetS) which includes an umbrella of metabolic conditions as insulin resistance (IR), dyslipidemia, hyperglycemia, hypertension, and cardiovascular disease (CVD) [6-8].

In the earliest MASLD stages, mitochondria conquer an ascertained role by engaging a strategy called "mitochondrial flexibility" through which they adapt number, mass, and activity by harmonizing their lifecycle and turnover which includes fusion, fission and mitophagy [9, 10]. The liver is enriched in mitochondria, ranging from 500 to 4000 number *per* hepatocyte, and these organelles are crucial for whole-body homeostasis and liver physiology since they provide energy by oxidative phosphorylation (OXPHOS), β-oxidation, tricarboxylic acid (TCA) cycle and ketogenesis [11-14]. Mitochondria cannot be generated *de novo* and their shaping leads to the fusion-fission interchange regulated by the peroxisome proliferator-activated receptor (PPAR)-γ coactivators 1 (PGC1α) which also orchestrates OXPHOS capacity, heme biosynthesis, glucose, and lipid metabolism [9, 15]. During MASH, the mitochondrial adaptability is lost paralleled by the assembly of misshapen and unfunctional mitochondria thus resulting in impaired β-oxidation, bioenergetic activity, ketogenesis and adenosine triphosphate (ATP) production [9]. Additionally, lower levels of mitophagy prompt the hepatic accumulation of failed mitochondria that consequently heighten the hepatocellular injury by triggering oxidative stress, inflammation, and release of mitochondrial damage-associated molecular patterns (Mito-DAMPs) among which the mitochondrial DNA (mtDNA) fragments (ccf-mtDNA) are the major component [16].

Recently, an oral, liver-directed, thyroid hormone receptor beta–selective agonist named Resmetirom has been approved by FDA for the treatment of biopsy-proven MASH. Data driven by a Phase 3 trial showed that 29% and 25% of patients who received Resmetirom, had MASH resolution and fibrosis improvement by at least one stage, respectively [17].

However, it represents the first and only medication for the treatment of MASH and no other therapeutic approach is available for MASLD prevention and for the management of at-risk patients. Lifestyle interventions encompassing low caloric diet and physical activity are the still pillars for the disease treatment, however the scant compliance of patients outlined the

urgent need for MASLD pharmacotherapy [18]. To date, hepatic biopsy is considered the gold standard procedure for the diagnosis and staging of MASLD, since it allows to delineate the degree of steatosis, necroinflammation and ballooning through the scoring system NAFLD Activity Score (NAS) [19, 20]. Nonetheless, it exhibits several limitations due to its low applicability, high cost, sample size and repeatability, that in turn could decline the diagnostic accuracy in some patients and children. Hence, facing the growing prevalence of MASLD alongside the pour diagnostic and therapeutic strategies, newly non-invasive methodological approaches have been proposed to estimate the severity of liver disease. Considering the key role of mitochondrial maladaptation over MASLD spectrum, emerging evidence emphasizes that the boosted release of ccf-mtDNA in the circulation accurately estimates the state of organelles dysfunction alongside the advanced liver injury, pointing at it as a promising non-invasive tool for identifying patients at risk of progressive MASLD [16]. To corroborate the key role that mitochondrial-related biomarkers may play, in the last years the focus switched to the exploration of real-time energy changes in both hepatic and peripheral blood [21, 22].

Although environment largely impacts on MASLD onset, it has also a strong heritable component and 50-70% of the individual susceptibility to develop the disease alongside its phenotypic variability are owed to inherited risk factors [23-26]. Recently, we have demonstrated that the co-presence of the single nucleotide polymorphisms (SNPs) in patatin-like phospholipase domain-containing 3 (*PNPLA3*), transmembrane 6 superfamily member 2 (*TM6SF2*) and membrane bound o-acyltransferase domain-containing 7 (*MBOAT7*) hugely predisposes to progressive disease, highlighting the relevance of polygenic risk scores to assess MASLD advancement [27-31]. To investigate the impact of these genetic variations alone or combined over MASLD pathogenesis, the hepatoma cells (HepG2), homozygous for the I148M PNPLA3 variant were knocked-out (KO) for *MBOAT7* (MBOAT7$^{-/-}$), *TM6SF2* (TM6SF2$^{-/-}$), or both genes (MBOAT7$^{-/-}$TM6SF2$^{-/-}$) through the clustered regularly interspaced short palindromic repeats/CRISPR-associated protein 9 (CRISPR/Cas9) technology in order to mimic the human proteins loss-of-function. Interestingly, we found that the silencing of these genes and more so when in combination (double KO) disrupts the mitochondrial morphology, increases the organelles content, and triggers the oxidative damage, thus suggesting their involvement in mitochondrial dysfunction and possibly explaining their contribution to progressive MASLD [27, 32].

Therefore, to deepen the genetics engagement in the mitochondrial dysfunction, in the present study we firstly evaluated the mitochondrial dynamics in term of fusion/fission balance in HepG2 KO models. Secondly, we overexpressed the wild type (WT) proteins in KO cells thus benchmarking the latter with the new-obtained WT ones to explore whether TM6SF2 and/or MBOAT7 restoration improves mitochondrial dysfunction in term of morphology and function. For this purpose, we explored the mitochondrial lifecycle and activity alongside the consequent hepatocellular damage and metabolic reprogramming. Finally, in the translational perspective to use circulating non-invasive mitochondrial biomarkers to prognose disease severity in genetically predisposed individuals, we compared the hepatic and peripheral bioenergetic profiles in MASLD patients carrying *PNPLA3, MBOAT7* and/or *TM6SF2* variations.

Methods

Patients

We evaluated the ROS and H_2O_2 production, the mitochondrial complex I, III, IV and citrate synthase kinetic activities as well as respiration capacity in both frozen liver biopsies and PBMCs of 44 MASLD patients that were enrolled consecutively at the Metabolic Liver Diseases outpatient service at Fondazione IRCCS Cà Granda, Ospedale Maggiore Policlinico Milano (Milan, Italy). Inclusion criteria were the availability of a liver biopsy specimen for suspected MASH or severe obesity, DNA samples, and clinical data. MASH was defined by the concomitant presence of steatosis, lobular inflammation, and hepatocellular ballooning. Individuals with excessive alcohol intake (men, >30 g/d; women, >20 g/d), viral and autoimmune hepatitis, or other causes of liver disease were excluded. Informed written consent was obtained from each patient and the study protocol was approved by the Ethical Committee of the Fondazione IRCCS Ca' Granda, Milan and conforms to the ethical guidelines of the 1975 Declaration of Helsinki. Demographic, anthropometric, and clinical data of these patients are listed in **Table 1**. MASLD patients were stratified according to the genetic background, as follows: 0 for patients who had no risk variants; PNPLA3, MBOAT or TM6SF2 for the presence of GG, TT and TT alleles in homozygous in *PNPLA3*, *MBOAT7* or *TM6SF2* genes, respectively; 3NRV for subjects carrying all 3 at-risk variants either

heterozygous or homozygous. The peripheral blood mononuclear cells (PBMCs) were extracted from whole blood of MASLD patients and together with liver biopsies were homogenate in MAS buffer as described below

	Discovery cohort (n=44)
Sex, M	29 (65.9)
Age, years	52±13.89
BMI, kg/m2	28.61±4.08
IFG/T2D, yes	16 (36.36)
HOMA-IR	4.83±3.26
Insulin, IU/ml	22.27±17.80
Total cholesterol, mmol/L	5.01±0.98
LDL cholesterol, mmol/L	3.05±0.88
HDL cholesterol, mmol/L	1.31±0.28
Triglycerides, mmol/L	1.56±0.81
ALT, IU/l	4.04 {0.08-0.69}
AST, IU/l	3.64{3.52-3.76}
Moderate/mild, NAS	19 (43.2)
Severe, NAS	25 (56.8)
Number of Risk Variants (NRV)	
0 NRV	10 (22.7)
GG PNPLA3	11 (25.0)
TT MBOAT7	9 (20.5)
TT TM6SF2	7 (15.9)
3 NRV	7 (15.9)

Table 1: Values are reported as mean±SD, number (%) or median {IQR}, as appropriate. BMI: body mass index; IFG: impaired fasting glucose; T2D: type 2 diabetes; HDL: high density lipoprotein; LDL: low density lipoprotein; ALT: alanine aminotransferase; AST: aspartate aminotransferase; RV: risk variants. Characteristics of participants were compared across histological clinical phenotype using linear regression model (for continuous variables) or logistic regression model (for categorial characteristics). Variables with skewed distribution were logarithmically transformed before analyses. 0: indicates the absence of risk variants; 1-2-3 indicates the total number of risk variants carried.

Histologic Evaluation

Steatosis was divided into the following 4 categories based on the percentage of affected hepatocytes: 0, 0%–4%; 1, 5%–32%; 2, 33%–65%; and 3, 66%–100%. Disease activity was

assessed according to the NAFLD activity score (NAS), with systematic evaluation of hepatocellular ballooning and necroinflammation; fibrosis also was staged according to the recommendations of the NAFLD Clinical Research Network [20]. The scoring of liver biopsy specimens was performed by independent pathologists unaware of patient status and genotype. MASH was diagnosed in the presence of steatosis, lobular necroinflammation, and hepatocellular ballooning. Patients were stratified based on the clinical assessment of both MASH and fibrosis (MASH-fibrosis).

Genotyping

The MASLD patients were genotyped in duplicate for the rs738409 C>G (PNPLA3 I148M), rs58542926 C>T (TM6SF2 E167K), and rs641738 C>T MBOAT7 risk variants using TaqMan 5'-nuclease assays (**Tables S1A)** (Life Technologies, Carlsbad, CA) as already described [33, 34].

Sample collection, storage, and homogenization

Frozen liver biopsies (1 to 3 mg) were manually homogenized in 250 µl MAS buffer (70 mM sucrose, 220 mM mannitol, 5 mM KH2PO4, 5 mM MgCl2, 1 mM EGTA, 2 mM HEPES). Then, centrifuge homogenates 5 min at 1000 × g, 4°C. Collect the resulting supernatant as the homogenate sample and discard the pellet. The supernatant (tissue homogenate) may be stored at −80°C for long-term storage.

300 µl of frozen whole blood were aliquoted in a new Eppendorf, it was added 900 µl of PBS 1X (1:3) and centrifuge 10 min at 100 x g, 18-24°C without break. Discard the supernatant and add 2 mL PBS 1X to resuspend the pellet of PBMCs. Centrifuge 100 x g 10 min at 100 x g, 18-24°C without break, discard the supernatant e resuspend the PBMCs pellet in 300 µl MAS buffer. The PBMCs homogenate may be stored at −80°C for long-term storage. Both liver biopsies and PBMCs homogenate in MAS buffer were quantified through BCA assay.

Frozen liver tissues and PBMCs respirometry: Seahorse assay

Based on BCA normalization, loaded 80 µg of liver biopsies and PBMCs homogenate in MAS buffer in a Seahorse XF24 plate and added 20 µl MAS buffer. Centrifuge the loaded plate 5 min at 2000 × g, 4°C without brake, using a plate carrier. Add 350 µl MAS buffer containing cytochrome c (10 µg/ml, final concentration) to allow complete membrane permeabilization

to the substrates. Prepare the cartridge by injecting 70 μl of different drugs as follow: port A: NADH (1 mM) (Complex I substrate) for complex I assessment, or 5 mM succinate (Complex II substrate) + 2 μM rotenone (Complex I inhibitor) for Complex II assessment; port B: Antimycin A (4 μM) (Complex III inhibitor); port C: TMPD (Electron donor to cytochrome c/Complex IV) + ascorbic acid (Maintains TMPD in the reduced state) (0.5 mM TMPD + 1 mM ascorbic acid); port D: Azide (Complex IV inhibitor) (50 mM). All compound injections should be diluted in MAS buffer. The measure times for the Seahorse run protocol was customized as follow: cycle 1: wait 2 min, mix 2 min, wait 2 min; measurement period 1: mix 50 sec, measure 4 min (x 4 cycles); injection 1 (port A), measure after injection: mix 50 sec, measure 4 min (x 4 cycles); injection 2 (port B), measure after injection: mix 50 sec, measure 4 min (x 4 cycles); injection 3 (port C), measure after injection: mix 50 sec, measure 4 min (x 4 cycles); injection 4 (port D), measure after injection: mix 50 sec, measure 4 min (x 4 cycles). The Maximal respiratory capacity was calculated as follow: through complex I: $OCR_{NADH} - OCR_{antimycin}$; through complex II: $OCR_{succinate+rotenone} - OCR_{antimycin}$; through complex IV: $OCR_{TMPD+Ascorbate} - OCR_{azide}$.

Mito Tracker staining

A total of 1×10^5 cells were seeded on coverslips lodged in a 6-well plate in duplicate and kept overnight in DMEM containing 10% FBS, 1% L-glutamine, and 1% penicillin/streptomycin. After 24 hours, growth media was removed and cells were kept for 24 hours in quiescent medium, containing 0.5% bovine serum albumin (BSA), 1% L-glutamine, and 1% penicillin/streptomycin. The day after, cells were incubated with the MitoRed dye-working solution (Abcam, Cambridge, UK) for 30 minutes in a 37°C 5% CO2 incubator. Then, cells were washed twice with PBS 1X and fixed in 4% formalin for 20 minutes covered by lights. Finally, coverslips samples were mounted with a drop of aqueous VectaMount AQ Mounting Medium (Maravai LifeSciences, Inc, San Diego, CA) and observed at confocal structured illumination microscopy (SIM) using a 100X oil immersion and pinhole of 1.2 to view the mitochondrial network number and morphology. The MitoRed-positive-area was quantified by ImageJ software in 10 random micrographs (magnification, 60X) by calculating the MitoRed-positive area as a percentage of pixels above the threshold value with respect to the total pixels per area. The MitoRed-positive-area of different mitochondrial shape was

measured through ImageJ software in 10 random micrographs (magnification, 60X) by assessing 2 threshold value of MitoRed-positive area of *spaghetti*-like and globular mitochondria and then calculated the percentage of pixels above each threshold value with respect to the total pixels per area.

Transmission Electron Microscopy (Tem)

Cells were cultured as monolayer (70%–80% confluent) and trypsinized to obtain cell suspension. Cells were fixed with an aldehyde mixture (4% paraformaldehyde þ 2.5% glutaraldehyde in cacodylate buffer: pH 7.4) at 4C overnight. After primary fixation, cells were washed repeatedly with cacodylate buffer and were postfixed in 1% osmium tetroxide (OsO4) for 2 hours in the dark. Next, samples were left in 1.5% potassium ferrocyanide dissolved in 0.1 mol/L cacodylate for 1 hour on ice. Each sample was stained with 0.5% 5-uranyl acetate in water overnight. Finally, samples were dehydrated with increasing ethanol series, embedded in an Epon resin, and polymerized in an oven at 60C for 48 hours. Ultrathin (70–90 nm) sections were collected on nickel grids and observed with a Zeiss Leo 912 AB Omega TEM (Freiburg, Germany).

Quantification of mtDNA (D-loop) content

Genomic and mtDNA were extracted from cell lysates through QIAmp DNA Mini Kit (Manchester, UK). $2x10^6$ cells were resuspended in a Protease solution and incubated 56°C for 10 minutes to disruptprotein-DNAinteractions. Total DNA was trapped onto the QIAamp silica membrane, while contaminants were removed in the flowthrough. Subsequently, DNA was eluted in water and its concentration and quality were assessed by Nanodrop 1000 microvolume 42 spectrophotometer (ThermoFisher Scientific, U.S.A.). 5 ng/µl of DNA was used to quantify the amount of mtDNA. Specifically, we measured D-loop expression, the replication start site of the mtDNA, through TaqMan Assay. RNAse-P, a sequence known to exist in two copies in human genome, was used as a reference gene and both D-loop and RNase-P probes (**Table S1A**) run simultaneously. Median ΔCT per assay value was used as calibrator.

Quantification of ccf-mtDNA content

A total of 3 x 10^6 of cells were culture in DMEM containing 10% FBS, 1% L-glutamine, and 1% penicillin/streptomycin. After 24 hours, growth media was removed and cells were kept for 24 hours in quiescent medium, containing 0.5% bovine serum albumin (BSA), 1% L-glutamine, and 1% penicillin/streptomycin. The day after, the medium was collected and concentrated with Vivaspin® 2 Centrifugal Concentrator (Sartorius, Göttingen, Germany) to extract and purified DNA fragments by using QIAmp DNA Blood Mini Kit (Manchester, UK). The Protease solution and AL Buffer were added to 150 µL concentrated cells media and incubated 56°C for 10 minutes to disrupt protein-DNA interactions. The DNA fragments up to 50 kb were trapped in columns providing silica membrane followed by two rinsing steps, while contaminants were removed in the flowthrough. Subsequently, DNA was eluted in water and its concentration and quality were assessed by Nanodrop 1000 microvolume 42 spectrophotometer (ThermoFisher Scientific, U.S.A.). 20 ng/µl of DNA was used to quantify the amount of ccf-mtDNA. Quantitative real-time PCR was performed by an ABI 7500 fast thermocycler (Life Technologies), using SYBR Green chemistry (Fast SYBR Green Master Mix; Life Technologies–ThermoFisher, Carlsbad, CA) and COXIII and ND1 primers listed in **Table S1B**. Specifically, the thermocycling setup was set as follow: 95°C for 10 minutes, 40 cycle: 95°C for 10 minutes, 60°C for 1 minute, 95°C for 15 second, 60°C for 1 minute and 95°C for 15 second. All reactions were delivered in quadruplicate. Data were normalized on the standard curve obtained from serial dilutions of a sample pool at known concentration to measure the quantity (gram) of DNA. Then, the amount of ccf-mtDNA (gram/150 µL), encompassing the sum of COXIII and ND1 quantities, was divided with the size of PCR fragments (bp; 102 bp COXIII, 109 bp ND1) and the molar mass per base pair (g mol^{-1}) [35]. The product was finally multiplied with Avogadro's constant to obtain the quantity (picogram) of DNA fragments expressed as logarithmic. Results were represented as mean and standard error (SE) and graphed as data points.

Statistical Analysis

For descriptive statistics, continuous variables were reported as means and SD or as the median and interquartile range for highly skewed biological variables. Variables with skewed distribution were logarithmically transformed before analyses. The frequencies for each risk

variant subgroup were compared using the chi-squared test. Differences between groups were calculated by 1-way nonparametric ANOVA (Kruskal–Wallis), followed by post hoc *t* test (2-tailed) when 2 groups were compared, or the Dunn multiple comparison test when multiple groups were compared, adjusted for the number of comparisons. *P* values less than .05 were considered statistically significant. Statistical analyses were performed using JMP 16.0 (SAS, Cary, NC) and Prism software (version 9.0, GraphPad Software, San Diego, CA).

Results

Restoring MBOAT7 and/or TM6SF2 wild-type activities in knock-out (KO) models rebalances the mitobiogenesis

It is well established that the impaired mitochondrial number and architecture result from unbalanced mitobiogenesis and flow towards maladaptive organelles activity. We recently demonstrated that *PNPLA3*, *MBOAT7* and *TM6SF2* loss-of-functions affects the mitochondrial morphology and biomass, although we didn't provide any data regarding their impact on organelle's dynamics [27]. Therefore, in this study we firstly investigated the mechanisms through which genes deletion may impair mitochondrial lifecycle by exploiting HepG2 MBOAT7$^{-/-}$, TM6SF2$^{-/-}$ and MBOAT7$^{-/-}$ TM6SF2$^{-/-}$ models.

Then, we restored the WT proteins through a lentiviral transfection in KO cells aiming to obtain stable cell lines that overexpress MBOAT7 (MBOAT7$^{+/+}$) and/or TM6SF2 WT (TM6SF2$^{+/+}$; MBOAT7$^{+/+}$ TM6SF2$^{+/+}$) genes (**Figure S1A-F**) and to assess whether their contribute to mitochondrial dynamics, maladaptive function, metabolic reprogramming, and advanced injury may be reversed.

As evidence that the activity of MBOAT7 and TM6SF2 had been restored, lipid accumulation, evaluated by ORO staining (**Figure S1G-H)** and triglycerides (**Figure S1I)**/cholesterol (**Figure S1J)** content, was reduced in MBOAT7$^{+/+}$, TM6SF2$^{+/+}$ and MBOAT7$^{+/+}$ TM6SF2$^{+/+}$ cells (**Figure S1G-J).**

Protein (**Figure 1A-B**) and mRNA (**Figure S2A**) levels of PGC1α, key regulator of mitochondrial lifecycle and β-oxidation, increased in MBOAT7$^{-/-}$ cells and much more in

TM6SF2$^{-/-}$ and MBOAT7$^{-/-}$ TM6SF2$^{-/-}$ones (adjusted **p<0.01, *p<0.05 *vs* Cas9) as a counter strategy in response to lipid overload (**Figure S1G-J**). In keeping with reduced lipid accumulation, the restore of MBOAT7 and TM6SF2 WT proteins declined PGC1α levels showing the strongest effect in MBOAT7$^{+/+}$TM6SF2$^{+/+}$ cell line (**Figure 1A-B, Figure S2A**: adjusted **p<0.01 *vs* MBOAT7$^{-/-}$, TM6SF2$^{-/-}$; adjusted *p<0.05 *vs* MBOAT7$^{-/-}$TM6SF2$^{-/-}$). Concerning mitochondrial fusion, Mfn1 (**Figure 1A; Figure S2B-F**), Mfn2 (**Figure S2C-G**) and Opa1 (**Figure 1A; Figure S2H**) levels were lower in KO cells and mostly in MBOAT7$^{-/-}$ TM6SF2$^{-/-}$ model whereas they were restored in WT cells and especially in MBOAT7$^{+/+}$TM6SF2$^{+/+}$ ones (adjusted *p<0.05 *vs* MBOAT7$^{-/-}$, TM6SF2$^{-/-}$, MBOAT7$^{-/-}$ TM6SF2$^{-/-}$). mRNA expression and protein activity of DRP1 (**Figure 1A; Figure S2D-I**) and Fis1 (**Figure 1A; Figure S2E**), which are involved in mitochondrial fission, were higher in MBOAT7$^{-/-}$ TM6SF2$^{-/-}$ cells while they returned under physiological condition in WT overexpressed models (adjusted *p<0.05 *vs* Cas9, MBOAT7$^{-/-}$ TM6SF2$^{-/-}$; adjusted **p<0.01 *vs* MBOAT7$^{-/-}$, TM6SF2$^{-/-}$, *MBOAT7*$^{-/-}$ TM6SF2$^{-/-}$). Finally, the silencing of MBOAT7 and TM6SF2 alone and much more of both repressed the mitophagy pathway exhibiting vacuolar autophagic structures, that was recovered in WT cells and especially in MBOAT7$^{+/+}$TM6SF2$^{+/+}$ clones (**Figure 1C-F).** Taken together, these data suggest that the concurrent MBOAT7 and TM6SF2 deletion hugely unbalances the mitochondrial lifecycle towards high fission and inoperative mitophagy, which explains the increased mass of organelles and the accumulation of misfolded ones in the KO models. The latter were confirmed by confocal microscopy (**Figure 2A-B**) and D-loop copies assessment which reflects the mitochondrial mass (**Figure 2C**). Conversely, the total number of organelles was lower in WT models and especially in MBOAT7$^{+/+}$ TM6SF2$^{+/+}$ clones (adjusted **p<0.01 *vs* Cas9, MBOAT7$^{-/-}$, TM6SF2$^{-/-}$, MBOAT7$^{-/-}$ TM6SF2$^{-/-}$) (**Figure 2A-B)** thus suggesting that the restore of protein activities resets mitobiogenesis possibly ensuring the assembly of physiological mitochondria (referred to as *spaghetti*-like).

The restore of MBOAT7 and/or TM6SF2 wild-type proteins in knock-out models reinstitutes mitochondrial morphology

The aberrant bulk of mitochondria is accompanied by an altered morphology. Indeed, we pointed out that KO cells exhibited many misshapen globular mitochondria compared to the

physiological *spaghetti*-like observed in WT overexpressed models (**Figure 2D**), supporting the notion that TM6SF2 and MBOAT7 deletion led to deranged mitobiogenesis paralleled by a suppressed mitophagy (**Figure 1-Figure S2**) **(**adjusted *p<0.05 *vs* Cas9, MBOAT7$^{-/-}$, MBOAT7$^{-/-}$ TM6SF2$^{-/-}$; adjusted **p<0.01 *vs* TM6SF2$^{-/-}$, MBOAT7$^{-/-}$ TM6SF2$^{-/-}$). Consistently with the re-established mitochondrial plasticity in WT overexpressed cells, the organelles appeared more elongated showing regular double membranes and cristae architecture (**Figure 2E**). Therefore, we could enhance the theory that the higher number of mitochondria is not exclusively representative of an enhanced organelles function but it may be related to imbalanced life cycle.

The re-establishment of MBOAT7 and/or TM6SF2 wild-type activities in knock-out cells rescues mitochondrial function

To assess whether the overexpression of MBOAT7 and TM6SF2 rescues organelles' function, we firstly evaluated mRNA levels of *PPARα* (**Figure 3A**), master regulator of FFAs oxidation. The WT overexpressed cell lines showed higher expression of *PPARα*, thus demonstrating that the steatotic phenotype was attenuated after MBOAT7 and/or TM6SF2 restore (**Figure S1**). Concerning mitochondrial respiration and Krebs cycle, the OXPHOS capacity (**Figure 3B**) alongside the activity of complexes III and IV, ATP synthase and citrate synthase (**Figure S3A-D**), they were decreased in KO cells and mainly in MBOAT7$^{-/-}$ TM6SF2$^{-/-}$ ones, in keeping with low mitochondrial fusion (**Figure 1A-Figure S2B-C-F-G-H**). Conversely, their levels were restored in WT overexpressed models especially in MBOAT7$^{+/+}$ TM6SF2$^{+/+}$ clone in agreement with a balanced mitobiogenesis (**Figure 1-S2**) and physiological mitochondrial plasticity (**Figure 2**) (adjusted **p<0.01 *vs* Cas9, MBOAT7$^{-/-}$ TM6SF2$^{-/-}$; adjusted *p<0.05 *vs* Cas9, TM6SF2$^{-/-}$, MBOAT7$^{-/-}$ TM6SF2$^{-/-}$). The quantitative measurement of the total ATP rate derived from mitochondrial and glycolytic pathways revealed that the mitochondrial oxygen consumption rate (OCR) which was lower in MBOAT7$^{-/-}$ TM6SF2$^{-/-}$ clone, increased in WT overexpressed models and mostly in MBOAT7$^{+/+}$ TM6SF2$^{+/+}$ cells (**Figure 3C-D**) (adjusted *p<0.05 *vs* Cas9, MBOAT7$^{-/-}$, TM6SF2$^{-/-}$, MBOAT7$^{-/-}$ TM6SF2$^{-/-}$). Consistently, the ATP production derived equally from glycolytic pathway and mitochondria in all KO cell lines unless for the MBOAT7$^{-/-}$ TM6SF2$^{-/-}$ clone which showed the highest extracellular acidification rate (ECAR) as energy source from anaerobic glycolysis (**Figure 3E-F**) (adjusted **p<0.001, *p<0.05 *vs* own ATP glycolysis). Contrarywise, the upregulation of MBOAT7 and

TM6SF2 WT activities alone and mainly combined enhanced the ATP production related to OXPHOS capacity, thus recovering the mitochondrial functions, and impeding the metabolic reprogramming which is hallmark of tumorigenesis (**Figure S4**).

The overexpression of MBOAT7 and/or TM6SF2 wild-type forms in knock-out cells attenuates the advanced hepatocellular damage due to mitochondrial failure

The switch toward anaerobic glycolysis (**Figure 3-Figure S3**) is one of the first key step in the malignant transformation paralleled by high proliferation capacity and invasiveness (**Figure S4**). In support to this notion, KO models and particularly the MBOAT7$^{-/-}$ TM6SF2$^{-/-}$ clone converted the glucose into lactate by triggering lactate dehydrogenase (LDH) activity and production, both reduced in WT overexpressed models (**Figure 4A-C**) (adjusted *$p<0.05$ *vs* Cas9, TM6SF2$^{-/-}$; adjusted **$p<0.01$ *vs* MBOAT7$^{-/-}$, MBOAT7$^{-/-}$TM6SF2$^{-/-}$). Lactate directly takes part in oxidative damage resulting in boosted Reactive Oxygen Species (ROS)/Reactive nitrogen species (ROS/RNS) ratio, ROS-induced DNA damage and malondialdehyde (MDA) production which were observed mostly in MBOAT7$^{-/-}$TM6SF2$^{-/-}$ cells, whereas they strongly decreased after the MBOAT7 and/or TM6SF2 WT upregulation (**Figure 4D-F**) (adjusted *$p<0.05$, **$p<0.01$ *vs* Cas9, MBOAT7$^{-/-}$, TM6SF2$^{-/-}$, MBOAT7$^{-/-}$TM6SF2$^{-/-}$). As a response to unbalanced mitobiogenesis (**Figure 1-S2**) and failed mitochondrial activity (**Figure 3-S3**), KO models released higher circulating cell-free mitochondrial DNA (ccf-mtDNA) which derives from damaged organelles (**Figure 4G**). Otherwise, the upregulation of MBOAT7 and/or TM6SF2 WT proteins greatly reduced the release of ccf-mtDNA (**Figure 4G**), corroborating the hypothesis that the high number of mitochondria is not representative of an enhanced function and that genetics directly impacts on the integrity of mitochondria. Hence, the assessment of ccf-mtDNA levels may strongly mirror mitochondrial derangement due to *TM6SF2* and *MBOAT7* deletion, thus paving the way to consider them as a mitochondrial circulating biomarker of progressive MASLD in genetically predisposed individuals.

The PNPLA3 I148M overexpression in hepatoma cells impairs the mitochondrial function

In our MASLD *in vitro* models, we deeply demonstrated that MBOAT7 and TM6SF2 loss-of-functions in HepG2 cells which carry the PNPLA3-I148M variant in homozygosity, conquered a key role in the mitochondrial maladaptation, exhibiting the strongest effect when both genes were deleted (MBOAT7$^{-/-}$TM6SF2$^{-/-}$). Moreover, the restore of MBOAT7 and TM6SF2 WT activities rescued the mitochondrial failure phenotype, corroborating their role in contributing to mitochondrial dysfunction encompassing tampered lifecycle, morphology, and activity.

As HepG2 cells carry the I148M mutation, we were not able to discriminate its effect on mitochondrial morphology and function from that of TM6SF2 and MBOAT7 in KO models. Interestingly, Cas9 cells carrying the I148M protein did not affect the organelles dynamics and function, hinting that PNPLA3 loss-of-function mutation may not play a role in the mitochondrial dysfunction. Nonetheless, literature evidence showed that the overexpression of I148M in hepatoma cells was correlated with mitochondrial maladaptation, suggesting the linkage between the upregulation of the mutated protein and organelles impairment [36]. Therefore, in order to investigate whether boosted I148M levels may alter the mitochondrial dynamics, we performed a lentiviral transfection in HepG2 (in order to force the mutation effect) and Hep3B (PNPLA3 WT) cells by using pLenti-C-mGFP-P2A-Puro lentiviral vectors (HepG2 I148M$^{+/+}$and Hep3B I148M$^{+/+}$). The vector deigns embraced a GFP tag fused with an ORF (PNPLA3-I148M) targeting the I148M protein that was upregulated in all cell lines (**Figure 5A-B**) (adjusted **$p<0.01$ *vs* HepG2 and Hep3B). At ORO staining, the lipid accumulation increased in Hep3B I148M$^{+/+}$ cells and more so in HepG2 I148M$^{+/+}$ ones, resulting in the assembly of larger LDs (**Figure 5C**). Concerning mitobiogenesis, PGC1α protein levels augmented in both overexpressed models suggesting a responsive strategy to counter fat accumulation (**Figure 5D**). About fusion process, the Opa1 activity was reduced in the overexpressed cell lines (**Figure 5D**) supported by lower OXPHOS capacity observed at Western Blot (**Figure 5E**). In keeping with these results, the ATP synthase activity, ATP content and citrate synthase activity decreased in all overexpressed cells, emphasizing that the I148M overexpression dampened the oxidative phosphorylation probably due to high lipid overload (**Figure 5F-H**) (adjusted ***$p<0.001$, **$p<0.01$ and *$p<0.05$ *vs* HepG2 and Hep3B). Consistently, the ROS/RNS ratio (**Figure 5I)** and LDH production (**Figure 5J)** were boosted in overexpressed cells alongside the release of ccf-mtDNA (**Figure 5K)**, supporting the

mitochondrial dysfunction (adjusted ***p<0.001, **p<0.01 and *p<0.05 *vs* HepG2 and Hep3B). To sum up, the induced upregulation of I148M-PNPLA3 protein in *in vitro* hepatoma cells, by resembling the overload of mutated protein in human carriers, unveiled its involvement in the organelle's maladaptation.

Hepatic and circulating mitochondrial activity is impaired in MASLD patients carrying the 3 at risk variants

Based on our *in vitro* results, the co-presence of *PNPLA3*, *MBOAT7* and *TM6SF2* loss-of-functions in HepG2 cells hugely impacts on mitochondrial plasticity exhibiting the restore of organelles' dynamics and function after the upregulation of WT proteins. The impaired mitochondrial morphology and activity are mirrored by the huge release of ccf-mtDNA. All in all, these genes have been identified as the main predictors of progressive MASLD which is featured by deranged mitochondria that in turn release ccf-mtDNA. Therefore, in order to translate these *in vitro* findings into the clinic and to corroborate the utility of mitochondrial molecules assessment as non-invasive biomarker, we evaluated and compared the mitochondrial activity in frozen liver biopsies and peripheral blood mononuclear cells (PBMCs) of 44 MASLD patients (Discovery cohort) stratified according to genetic background as follow: WT (n=11; 22.7%), homozygous for the I148M PNPLA3 (n=11; 25.0%), homozygous for the rs641738 MBOAT7 (n=9, 20.5%), homozygous for the E167K TM6SF2 (n=7, 15.9%), carrying all 3 at-risk variants (3NRV) in heterozygosis or homozygosis (n=7, 15.9%) (**Table 1**). Hepatic ROS (**Figure 6A-Table S3**) and H_2O_2 (**Figure 6B- Table S3**) production increased in GG *PNPLA3*, TT *MBOAT7* and TT *TM6SF2* carriers and even more in 3NRV ones (*p<0.05, **p<0.001 *vs* 0NRV). Interestingly, a comparable result was observed in PBMCs suggesting that their mitochondrial performance may reflect the hepatic one (**Figure 6A-B**). Concerning mitochondrial respiration, the total and kinetic activity of citrate synthase (**Figure 6C- Table S3-S4**), mitochondrial complex I (**Figure 6D- Table S3-S4**), mitochondrial complex III (**Figure 6E- Table S3-S4**) and ATP synthase (**Figure 6F- Table S3-S4**) were lower in both liver biopsies and PBMCs of GG *PNPLA3*, TT *MBOAT7* and TT *TM6SF2* individuals showing the main reduction in 3NRV carriers (*p<0.05, **p<0.001, ***p<0.0001 *vs* 0NRV). Therefore, in genetically susceptible MASLD patients the mitochondrial failure in the circulation closely mirrors that found in the liver.

The sera bioenergetic profile resembles the hepatic one and exhibits a strong prognostic value for MASLD severity in 3NRV carriers

In keeping with the impaired mitochondrial activity, we demonstrated that hepatic and sera OCR progressively decreased from I148M PNPLA3 carriers (30%), to rs641738 MBOAT7 (70%) or E167K TM6SF2 (80%) variations with the lowest levels in 3NRV individuals (90%) (***p<0.0001 *vs* 0NRV) (**Figure 7A-B**), thus resembling the declined OXPHOS capacity observed in MBOAT7$^{-/-}$TM6SF2$^{-/-}$ model (**Figure3-S3**). At multivariate analysis adjusted for age, sex, BMI and diabetes, the co-presence of 3NRV was independently associated with reduced respiration in terms of complex I/IV (**Table 2.** Liver biopsies: p=0.0001, β = -43.37, 95% CI, -64.81 to -21.92; PBMCs: p=0.002, β = -30.7, 95% CI, -49.96 to -11.45) and II/IV (**Table 3**. Liver biopsies: p=0.0001, β = -27.24, 95% CI, -10.47 to -14.02 PBMCs: p<0.0001, β = -20.08, 95% CI, -25.20 to -14.96). These data highlight that genetics directly compromises the circulating bioenergetic profile which closely reflects the hepatic mitochondrial respiration. To investigate whether impaired OCR could estimate mitochondrial failure and thereby progressive disease, patients of the Discovery cohort were stratified according to the presence of MASH-fibrosis. Liver biopsies and PBMCs samples of MASH-Fibrosis patients exhibited a significant OCR reduction in terms of complex I/IV and II/IV activities (**Figure 7C**) (*p, **p at two-way ANOVA). At nominal logistic regression analysis adjusted for 3NRV, the hepatic respiration capacity of CI/IV and CII/IV displayed a prognostic value for MASH-Fibrosis of 76% and 79%, respectively (**Figure 7D**). Intriguingly, the sera OCR-CI/IV and OCR-CII/IV unveiled a competitive prediction capacity for MASH-Fibrosis of 85% and 84% (**Figure 7D**). Therefore, the clinical evidence confirmed the *in vitro* results thus reinforcing the applicability of mitochondrial circulating molecules (i.e. ccf-mtDNA) as non-invasive biomarkers of progressive MASLD in genetically predisposed individuals.

Discussion

In the present study, we examined the relationship between genetics and mitochondrial dysfunction, both guilty players in MASLD pathogenesis [9, 23, 27]. Nowadays, MASLD is the most common chronic liver disorder worldwide and liver biopsy still remains the gold standard method for the diagnosis of its progressive forms. Facing the growing MASLD

prevalence alongside scant diagnostic and therapeutic strategies, newly non-invasive methodological approaches have been proposed to estimate the severity of liver disease [16]. One of the key steps which features the MASLD switch towards MASH is the outbreak of mitochondrial abnormalities due to heighten fat accumulation. This results in unbalanced mitochondrial lifecycle that translates in aberrant mitochondrial number, morphology, and activity worsening progressive liver damage. The disequilibrium of mitobiogenesis alongside the consequent accumulation of failed mitochondria have been observed in hepatic tissues of both MASH individuals and murine models, thereby underling that MASLD may be considered as a mitochondrial disorder [9]. In furtherance, emerging evidence correlates the high release of ccf-mtDNA from hepatic damaged organelles alongside impaired serum respirometry with progressive MASLD stages, suggesting the applicability of mitochondrial circulating molecules as non-invasive biomarkers [16, 22].

MASLD is a multifactorial disease and exhibits a strong hereditable component [23, 37, 38]. We demonstrated that the co-presence of *PNPLA3*, *MBOAT7* and *TM6SF2* at-risk variants in 1380 MASLD subjects hugely predisposes to HCC development, highlighting the usefulness of a polygenic risk score to prognose disease severity. By exploiting a genetic *in vitro* model, we proved that the deletion of *MBOAT7* and *TM6SF2*, alone and mostly combined, overflowed intracellular lipid accumulation and in parallel triggered the mitochondrial derangement in terms of morphology and activity, thereby contributing to advanced hepatic damage [27].

Since MASLD occurs as a mitochondrial disease and PNPLA3, MBOAT7 and TM6SF2 loss-of-functions seem to achieve a role in organelles dysfunction, in this study we firstly explored whether the restoring of the WT proteins could improve mitochondrial activity and morphology by exploiting an *in vitro* model. The second challenging outcome was to compare the hepatic bioenergetic profile with the circulating one in patients carrying the three at risk variants with the finale purpose to define a prognostic signature of progressive MASLD in these individuals.

Therefore, we performed a lentiviral transfection to overexpress *MBOAT7* and *TM6SF2* WT proteins alone or in combination in HepG2 KO cells. The WT overexpressed models strongly reduced the intracellular fat accumulation similarly to what was reported by Sharpe and colleagues in male C57BL6/J-MBOAT7$^{+/+}$ mice and by Pant et al in Huh-7-TM6SF2 WT$^{+/+}$ cells

[39, 40]. Interestingly, the WT overexpression of *MBOAT7* or *TM6SF2* in MBOAT7$^{-/-}$TM6SF2$^{-/-}$ clone brought out a glass effect resulting in a more conspicuous lipid reduction in MBOAT7$^{+/+}$TM6SF2$^{-/-}$ than MBOAT7$^{-/-}$TM6SF2$^{+/+}$. This data corroborated the linkage between macro steatotic phenotype and MBOAT7 loss-of-function protein already demonstrated in MBOAT7$^{-/-}$ cell line, resulting in the shift of phosphatidylinositols toward the synthesis of saturated and monounsaturated triacylglycerols with the consequent induction of DNL [30]. Contrariwise, the *TM6SF2* KO induced the formation of smaller lipid droplets (LDs) by increasing the synthesis of triacylglycerols enriched in saturated and monounsaturated fatty acid chains [27].

As above mentioned, *TM6SF2* and *MBOAT7* KO models, more so when combined, impair the mitochondrial morphology and biomass, suggesting that these genetic variations may affect the organelles dynamics [27]. Consistently, in the present study, we observed that the deletion of *MBOAT7* or *TM6SF2* alone and mainly together promoted fission while inhibited both fusion and mitophagy, showing an unbalanced mitobiogenesis and an increased assembly of misshapen and failed organelles as described by Shami *et al* in hepatic biopsies of MASLD patients [41]. Conversely, the *MBOAT7* and *TM6SF2* WT co-overexpression rebalanced the mitochondrial life course, thus ensuring a physiological organelles morphology, architecture, and activity. These results corroborate the theory according to which the high number of mitochondria may correlate with impaired organelles' dynamics and progressive MASLD [42-45]. An increased mitochondrial biomass due to the accumulation of globular mitochondria in KO cell lines unlike the physiological *spaghetti-like* shaped in WT overexpressed cells, did not mirror a higher activity of the organelles. In keeping with this data, fibrotic mice fed with a high-trans-fat, high-fructose, and high-cholesterol (AMLN) diet, showed an increased number of disrupted mitochondria which were featured by low OXPHOS capacity, loss of cristae architecture and reduced expression of *Mnf1* and *Opa1*, thus underling the correlation between unbalanced mitochondrial lifecycle, impaired mitochondrial function and advanced liver damage [46]. In furtherance, Zahng et al demonstrated that *Mnf1* expression was reduced in 34 HCC patients and in MHCC97-H cells and inhibited cell proliferation, migration, and invasion, thereby playing a crucial role in impeding HCC development [47].

In another study, MASH patients showed high mitochondrial diameters, intra-mitochondria crystalline inclusions and granules in the matrix, which correlated with both mitochondrial swelling and OXPHOS failure [48]. Previous evidence has reported that in hepatic tissue of patients and animal models with MASLD, the mitochondrial respiratory chain capacity is reduced. Compared to healthy individuals, patients with MASLD have a reduction in respiratory chain activity of 37% in complex I, 42% in complex II, 30% in complex III, 38% in complex IV, and 58% in complex V [49, 50]. Consistently, we observed that *MBOAT7* and *TM6SF2* double KO decreased OXPHOS capacity, ATP production, ketogenesis and β-oxidation. The mitochondrial activity was rescued by the overexpression of the WT proteins which in turn led to a reduced release of ccf-mtDNA. Moreover, KO cells promoted the tumorigenic switching in terms of anaerobic glycolysis, proliferation, and invasiveness, that was strongly attenuated in WT overexpressed models characterized by recovered mitochondrial functions.

Notably, we found that the TM6SF2 loss-of-function more than MBOAT7 one may be mostly involved in the mitochondrial derangement by further prompting the total number of misshapen and failed mitochondria. In corroboration with our results, it has been demonstrated that the TM6SF2 deficiency reduced the amount of polyunsaturated fatty acids (PUFAs), along with alterations in mitochondrial β-oxidation in Huh-7 cells, whereas it induced changes in endoplasmic reticulum architecture in the small intestine of zebrafish, supporting the notion that TM6SF2 loss-of-function impacted both organelles' morphology and activity [51, 52]. Concerning PNPLA3 polymorphism, Cas9 cells carrying I148M protein did not affect the mitochondrial dynamics. However, literature evidence reported that the overexpression of I148M in Huh-7 hepatoma cells was correlated with high levels of lactate and γ-glutamyl-amino acids, hallmarks of metabolic switching and mitochondrial dysfunction, respectively [36]. Therefore, in order to investigate the possible crosslink between PNPLA3 loss-of-function and organelles maladaptation, we upregulated the I148M mutated protein in HepG2 cells in order to force the mutation effect and in Hep3B cells which were WT for the I148M variant ($HepG2^{I148M+/+}$ and $Hep3B^{I148M+/+}$). The *in vitro* I148M overexpression, which mimicked the I148M upregulated transcription in human carriers, enhanced the LDs accumulation and reduced the mitochondrial functions in terms of OXPHOS rate and ATP reduction in both cell lines. This caused a boosted oxidative stress as

well as release of lactate and ccf-mtDNA, suggesting the I148M involvement in the mitochondrial failure.

To sum up, the *in vitro* results demonstrated that genetics impact on mitobiogenesis which echoed on impaired organelles content and activity, thus contributing to genetic-based MASLD progression. The dysfunctional metabolism encompassing mitochondrial aberrances, lipid accumulation and oxidative stress alongside genetic background lie at the center of MASLD pathogenesis [21]. High ccf-mtDNA levels in body fluids was correlated with advanced MASLD stages, underling the use of liquid biopsy as novel, non-invasive, cheaper, and repeatable MASLD diagnostic strategy [16].

Therefore, we tried to establish whether the circulating mitochondrial bioenergetic profile accurately reflects the hepatic one to support the validity of molecule derived from damaged mitochondria as biomarker of advanced disease in genetically predisposed individuals. Consistently with our *in vitro* findings, liver biopsies of 3NRV patients exhibited a strong reduction of mitochondrial activity resulting in low OXPHOS rate. Notably, the PBMCs bioenergetic profile thoroughly reflected the hepatic one, showing a strong prognostic value for MASH-Fibrosis in 3NRV carriers [22, 53, 54].

This study could open the spyhole towards the restore of PNPLA3, MBOAT7 and TM6SF2 activities to counteract MASLD by focusing on them as potential therapeutic targets at RNA level for personalized therapy. The targeting of PNPLA3 I148M variant in mice model by tri-antennary N-acetyl galactosamine (GalNAC3) conjugated with an antisense RNA oligonucleotide (ASO) decreased hepatic inflammation, steatosis, and fibrosis [55]. In another recent study, targeting Pnpla3 in the 148M knock-in mice by Adeno associated viral AAV-mediated shRNA reduced hepatic triglyceride contents [56].

Focusing on our results, the suitable approach could be gene therapy strategies based on the gene transfer that can introduce a WT copy to recover the function of the protein. For instance, the AAV-mediated delivery of a permanently active mutant form of human carnitine palmitoyl transferase 1A (hCPT1AM) in the liver of mice fed High Fat Diet to induce obesity and MASLD, enhanced liver fatty acid oxidation [57]. Furthermore, the AAV8-mediated gene transfer approach that allows long-term hepatic SIRT1 overexpression counteracted high carbohydrate diet-induced MASLD and improved whole-body metabolism in adult mice [58]. Supported by these literature evidence, we may delineate a new proof of concept regarding

the applicability of gene transfer therapy in genetic-based MASLD management to prevent of its progressive forms.

In addition, we firstly demonstrated that the circulating mitochondrial respirometry hugely resembles the hepatic one, exhibiting a strong prognostic power for MASH-fibrosis in 3NRV carriers.

To conclude, the novel aspects of this study are twofold. We confirmed the contribute of *PNPLA3*, *MBOAT7*, and *TM6SF2* loss-of-function variants to mitochondrial dysfunction that features progressive MASLD, suggesting that their restoration which reverses the failure phenotype may be a successful therapeutic strategy.

Secondly, we demonstrated for the first time that mitochondrial damage in PBMCs is the same as in the liver in MASLD patients thus suggesting in a pioneering fashion the use of circulating mitochondrial biomarkers (i.e. mt-ccf, bioenergetic index) to foresee disease severity in genetically predisposed individuals.

Table 2. Values are reported as mean±SD, number (%) or median {IQR}, as appropriate. BMI: body mass index; IFG/T2D: impaired fasted glucose/ type 2 diabetes; NRV: number of risk variants; β: beta coefficients; CI: confidence interval. $p<0.05$ was considered statistically significant. Generalized linear model adjusted for age, sex, BMI, and IGF/T2D and NRV=3.

	Liver biopsies	**PBMCs**

Seahorse complex I/IV	β {95% CI}	P value	β {95% CI}	P value
Age, Years	0.68 {-0.49-1.86}	0.25	0.78 {-0.35-1.92}	0.17
Sex, M	-19.37 {-36.10- -2.65}	**0.02**	-28.54 {-43.75- -13.33}	**0.0004**
BMI, Kg/m2	3.81 {0.15-7.47}	0.051	2.95 {-0.26-6.17}	0.07
IFG/T2D, yes	5.29 {-12.13-22.72}	0.54	-12.92 {-28.95-3.09}	0.11
NRV=3	-43.37 {-64.81- -21.92}	**0.0001**	-30.7 {-49.96- -11.45}	**0.002**

Table 3. Values are reported as mean±SD, number (%) or median {IQR}, as appropriate. BMI: body mass index; IFG/T2D: impaired fasted glucose/ type 2 diabetes; NRV: number of risk variants; β: beta coefficients; CI: confidence interval. $p<0.05$ was considered statistically significant. Generalized linear model adjusted for age, sex, BMI, and IGF/T2D and NRV=3.

Seahorse complex II/IV	Liver biopsies		PBMCs	
	β {95% CI}	P value	β {95% CI}	P value
Age, Years	-0.051 {-1.23-0.21}	0.16	-0.50 {-0.78- -0.22}	0.57
Sex, M	-0.16 [59]	0.97	1.72 {-2.27-5.71}	0.39
BMI, Kg/m2	0.42 {-1.83-2.67}	0.70	0.098 {-0.77-0.97}	0.82
IFG/T2D, yes	-4.14 {-14.89-6.59}	0.44	-2.27 {-6.45-1.89}	0.27
NRV=3	-27.24 {-10.47- -14.02}	**0.0001**	-20.08 {-25.20- -14.96}	**<.0001**

Figure legends

Figure 1. The MBOAT7 and/or TM6SF2 WT overexpression rebalances the mitochondrial lifecycle and turnover. **A-C-E)** The protein levels of PGC1α, Mfn1, Opa1, Drp1, Pink, Parkin, Bnip3-L, Bnip3, LC3 and phopsho-ubiquitin were assessed by Western blot and normalized to the vinculin housekeeping gene. **B-D)** Cytoplasmatic and nuclear localization of PGC1α and Parkin were represented by Immunocytochemistry pictures. **F)** Representative TEM images of autophagic structures in the form of vacuoles obtained by ultrathin 70-nm sections of hepatocytes. Black stars indicate the autophagic structures in the form of vacuoles in mitochondria and cytoplasm. At least 3 independent experiments were conducted. For bar graphs, data are expressed as means and SE. Adjusted $*P < .05$ and $**P < .01$.

Figure 2. The WT upregulation of MBOAT7 and/or TM6SF2 WT genes in knock-out models resumes the assembly of physiological shaped mitochondria. **A)** Representative confocal microscopy images (size range: 10 μm) of mitochondria obtained by Mito Tracker staining. **B)** Fluorescence Intensity per cells was quantified by ImageJ in 6 random nonoverlapping micrographs per condition by calculating the percentage of pixels above the threshold value in respect to total pixels per area. **C)** D-loop copies, that disclose intracellular number of mitochondria, were calculated by reverse-transcription quantitative PCR, and normalized to the RnaseP housekeeping gene. **D)** The ratio between spaghetti-like and globular shaped mitochondria per cells was quantified by ImageJ in 6 random nonoverlapping micrographs per condition by calculating the percentage of pixels above the threshold values of spaghetti-like and globular, respectively, in respect to total pixels per area. **E)** Representative TEM images of mitochondria obtained by ultrathin 70-nm sections of hepatocytes. Black arrows indicate the mitochondria. At least 3 independent experiments were conducted. For bar graphs, data are expressed as means and SE. Adjusted $*P < .05$ and $**P < .01$.

Figure 3. The MBOAT7 and/or TM6SF2 WT overexpression in knock-out models restore the mitochondrial functions. **A)** The mRNA expression of *PPARα* was evaluated by reverse-transcription quantitative PCR and normalized to the β-actin housekeeping gene. **B)** The protein levels of OXPHOS complexes I, II, III, IV and V were assessed by Western blot and normalized to the vinculin housekeeping gene. **C-D)** The oxygen consumption rate (OCR)

was obtained by Mito Stress test using the Seahorse XF Analyzers in live cells. **E-F)** The ATP rate derived from glycolysis and oxidative phosphorylation alongside the OCR/ extracellular acidification rate (ECAR) ratio were measured by Glycolytic Assay exploiting the Seahorse XF Analyzers in live cells. At least 3 independent experiments were conducted. For bar graphs, data are expressed as means and SE. Adjusted $*P < .05$ and $**P < .01$.

Figure 4. The MBOAT7 and/or TM6SF2 WT upregulation in knock-out cells attenuates the hepatocellular injury led to mitochondrial dysfunctions. **A)** The mRNA expression of *LDH* was evaluated by reverse-transcription quantitative PCR and normalized to the β-actin housekeeping gene **B)** The LDH activity was measured by the Lactate Dehydrogenase (LDH) Assay Kit in cell lysates. **C)** The LDH production was quantified through the LDH activity by Lactate Dehydrogenase (LDH) Assay Kit in cell supernatants. **D)** The oxidative stress was evaluated by Dichlorodihydrofluorescin (DCF) Reactive oxygen species/Reactive nitrogen species (ROS/RNS) Colorimetric Assay Kit in cell lysates. **E)** The ROS-induced DNA damage was detected through the DNA Damage Colorimetric Assay Kit (apurinic/apyrimidinic (AP) sites) in cell lysates. **F)** The malondialdehyde (MDA) production was calculated by the Lipid Peroxidation (MDA) Assay Kit in cell lysates. **G)** The release of cell-free mitochondrial DNA fragments (mt-ccf) was quantified through quantitative real-time PCR and normalized on the standard curve obtained from serial dilutions of a sample pool at known concentration. At least 3 independent experiments were conducted. For bar graphs, data are expressed as means and SE. Adjusted $*P < .05$ and $**P < .01$

Fig 5. The I148M PNPLA3 upregulation in hepatoma cells triggers the spontaneously lipid overload alongside mitochondrial failure. **A)** The mRNA expression of *PNPLA3* was evaluated by reverse-transcription quantitative PCR and normalized to the β-actin housekeeping gene. **B)** The protein levels of PNPLA3 tagged with GFP (PNPLA3-GFP) were assessed by Western blot and normalized to the vinculin housekeeping gene. **C**) LD accumulation was assessed by ORO staining (magnification, 630×). **D)** Cytoplasmatic and nuclear localization of PGC1α and Opa1 were represented by Immunocytochemistry pictures. **E)** The protein levels of OXPHOS complexes I, II, III, IV and V were assessed by Western blot and normalized to the vinculin housekeeping gene. **F)** The ATP5A (mtDNA–encoded subunit of the complex V) activity was quantified by ATP Synthase Enzyme Activity Microplate Assay

Kit in isolated mitochondria from cell lysates. **G)** The ATP production was quantified by ATP Colorimetric Assay in cell lysates. **H)** The citrate synthase activity was assessed through the Citrate Synthase Assay Kit in isolated mitochondria from cell lysates. **I)** The ROS-induced DNA damage was detected through the DNA Damage Colorimetric Assay Kit (apurinic/apyrimidinic (AP) sites) in cell lysates. **J)** The LDH production was quantified through the LDH activity by Lactate Dehydrogenase (LDH) Assay Kit in cell supernatants. **K)** The release of cell-free mitochondrial DNA fragments (mt-ccf) was quantified through quantitative real-time PCR and normalized on the standard curve obtained from serial dilutions of a sample pool at known concentration At least 3 independent experiments were conducted. For bar graphs, data are expressed as means and SE. Adjusted $*P < .05$ and $**P < .01$.

Figure 6. The mitochondrial activity is impaired in liver biopsies and PBMCs of 3NRV MASLD carriers. **A-B)** The oxidative stress was evaluated by Dichlorodihydrofluorescin (DCF) Reactive oxygen species/Reactive nitrogen species (ROS/RNS) Colorimetric Assay Kit in frozen liver biopsies and PBMcs. **C-D)** The complex I/III enzymatic activity was measured through a colorimetric assay in in frozen liver biopsies and PBMcs. **E)** The ATP5A (mtDNA–encoded subunit of the complex V) activity was quantified by ATP Synthase Enzyme Activity Microplate Assay Kit in in frozen liver biopsies and PBMcs. At least 3 independent experiments were conducted. For bar graphs, data are expressed as means and SE. Adjusted $*P < .05$ and $**P < .01$

Figure 7. The PBMCs bioenergetic profile reflect the hepatic one and exhibits a strong prognostic value for MASH-Fibrosis in 3NRV carriers. **A-B)** The oxygen consumption rate (OCR) was obtained by customized Seahorse assay using the Seahorse XF Analyzers in frozen hepatic biopsies and PBMCs. At least 4 independent experiments were conducted. For bar graphs, data are expressed as means and SE. Adjusted $*P < .05$ and $**P < .01$. **C)** At bivariate analysis patients with MASH-fibrosis exhibit lower OCR (Liver biopsies complexI/IV: P=0.01; Liver biopsies complexII/IV: P=0.004; PBMCs complexI/IV: P=0.001; PBMCs complexII/IV: P=0.01). **D)** The nominal logistic regression analysis corrected for 3NRV show that complexes I/IV and II/IV have a strong prognostic accuracy for MASH-Fibrosis (Liver biopsies

complexI/IV: AUC=76, P=0.0004; Liver biopsies complexII/IV: AUC=79, P=0.005; PBMCs complexI/IV: AUC=85, P=0.011; PBMCs complexII/IV: AUC=84, P=0.001)

Financial support: This study was supported by Italian Ministry of Health (Ricerca Corrente 2024 - Fondazione IRCCS Cà Granda Ospedale Maggiore Policlinico), by Italian Ministry of Health (Ricerca Finalizzata Ministero della Salute GR-2019-12370172; RF-2021-12374481) and by 5x1000 2020 RC5100020B).

Conflict of Interests: The authors declare that they have no conflict of interest.

References

1. Abd El-Kader, S.M. and E.M. El-Den Ashmawy, *Non-alcoholic fatty liver disease: The diagnosis and management.* World J Hepatol, 2015. **7**(6): p. 846-58.
2. Protopapas, A.A., et al., *Alcohol consumption in patients with nonalcoholic fatty liver disease: yes, or no?* Ann Gastroenterol, 2021. **34**(4): p. 476-486.
3. Marra, F., et al., *Molecular basis and mechanisms of progression of non-alcoholic steatohepatitis.* Trends Mol Med, 2008. **14**(2): p. 72-81.
4. Seen, T.K., et al., *Clinical indicators for progression of nonalcoholic steatohepatitis to cirrhosis.* World J Gastroenterol, 2021. **27**(23): p. 3238-3248.
5. Cholankeril, G., et al., *Hepatocellular carcinoma in non-alcoholic steatohepatitis: Current knowledge and implications for management.* World J Hepatol, 2017. **9**(11): p. 533-543.
6. Friedman, S.L., et al., *Mechanisms of NAFLD development and therapeutic strategies.* Nat Med, 2018. **24**(7): p. 908-922.
7. Dongiovanni, P., et al., *Nonalcoholic fatty liver disease or metabolic dysfunction-associated fatty liver disease diagnoses and cardiovascular diseases: From epidemiology to drug approaches.* Eur J Clin Invest, 2021. **51**(7): p. e13519.

8. Blachier, M., et al., *The burden of liver disease in Europe: a review of available epidemiological data.* J Hepatol, 2013. **58**(3): p. 593-608.
9. Longo, M., et al., *Remodeling of Mitochondrial Plasticity: The Key Switch from NAFLD/NASH to HCC.* Int J Mol Sci, 2021. **22**(8).
10. Longo, M., et al., *Mitochondrial dynamics and nonalcoholic fatty liver disease (NAFLD): new perspectives for a fairy-tale ending?* Metabolism, 2021. **117**: p. 154708.
11. Shum, M., et al., *Mitochondrial oxidative function in NAFLD: Friend or foe?* Mol Metab, 2021. **50**: p. 101134.
12. Galluzzi, L., O. Kepp, and G. Kroemer, *Mitochondria: master regulators of danger signalling.* Nat Rev Mol Cell Biol, 2012. **13**(12): p. 780-8.
13. Montemurro, C., et al., *Cell cycle-related metabolism and mitochondrial dynamics in a replication-competent pancreatic beta-cell line.* Cell Cycle, 2017. **16**(21): p. 2086-2099.
14. Degli Esposti, D., et al., *Mitochondrial roles and cytoprotection in chronic liver injury.* Biochem Res Int, 2012. **2012**: p. 387626.
15. Piccinin, E., G. Villani, and A. Moschetta, *Metabolic aspects in NAFLD, NASH and hepatocellular carcinoma: the role of PGC1 coactivators.* Nat Rev Gastroenterol Hepatol, 2019. **16**(3): p. 160-174.
16. Paolini, E., et al., *The Non-Invasive Assessment of Circulating D-Loop and mt-ccf Levels Opens an Intriguing Spyhole into Novel Approaches for the Tricky Diagnosis of NASH.* Int J Mol Sci, 2023. **24**(3).
17. Harrison, S.A., et al., *A Phase 3, Randomized, Controlled Trial of Resmetirom in NASH with Liver Fibrosis.* N Engl J Med, 2024. **390**(6): p. 497-509.
18. Roeb, E. and A. Geier, *Nonalcoholic steatohepatitis (NASH) - current treatment recommendations and future developments.* Z Gastroenterol, 2019. **57**(4): p. 508-517.
19. Nalbantoglu, I.L. and E.M. Brunt, *Role of liver biopsy in nonalcoholic fatty liver disease.* World J Gastroenterol, 2014. **20**(27): p. 9026-37.
20. Kleiner, D.E., et al., *Design and validation of a histological scoring system for nonalcoholic fatty liver disease.* Hepatology, 2005. **41**(6): p. 1313-21.
21. Ajaz, S., et al., *Mitochondrial dysfunction as a mechanistic biomarker in patients with non-alcoholic fatty liver disease (NAFLD).* Mitochondrion, 2021. **57**: p. 119-130.
22. Garrafa, E., et al., *Mitochondrial Dysfunction in Peripheral Blood Mononuclear Cells as Novel Diagnostic Tools for Non-Alcoholic Fatty Liver Disease: Visualizing Relationships with Known and Potential Disease Biomarkers.* Diagnostics (Basel), 2023. **13**(14).
23. Meroni, M., et al., *Genetics Is of the Essence to Face NAFLD.* Biomedicines, 2021. **9**(10).
24. Dongiovanni, P. and L. Valenti, *Genetics of nonalcoholic fatty liver disease.* Metabolism, 2016. **65**(8): p. 1026-37.
25. Dongiovanni, P., S. Romeo, and L. Valenti, *Genetic Factors in the Pathogenesis of Nonalcoholic Fatty Liver and Steatohepatitis.* Biomed Res Int, 2015. **2015**: p. 460190.
26. Dongiovanni, P., Q.M. Anstee, and L. Valenti, *Genetic predisposition in NAFLD and NASH: impact on severity of liver disease and response to treatment.* Curr Pharm Des, 2013. **19**(29): p. 5219-38.
27. Longo, M., et al., *TM6SF2/PNPLA3/MBOAT7 Loss-of-Function Genetic Variants Impact on NAFLD Development and Progression Both in Patients and in In Vitro Models.* Cell Mol Gastroenterol Hepatol, 2022. **13**(3): p. 759-788.
28. Bianco, C., et al., *Non-invasive stratification of hepatocellular carcinoma risk in non-alcoholic fatty liver using polygenic risk scores.* J Hepatol, 2021. **74**(4): p. 775-782.

29. Meroni, M., et al., *Mboat7 down-regulation by hyper-insulinemia induces fat accumulation in hepatocytes.* EBioMedicine, 2020. **52**: p. 102658.
30. Meroni, M., et al., *MBOAT7 down-regulation by genetic and environmental factors predisposes to MAFLD.* EBioMedicine, 2020. **57**: p. 102866.
31. Dongiovanni, P., et al., *PNPLA3 I148M polymorphism and progressive liver disease.* World J Gastroenterol, 2013. **19**(41): p. 6969-78.
32. Meroni, M., et al., *Expanding the phenotypic spectrum of non-alcoholic fatty liver disease and hypertriglyceridemia.* Front Nutr, 2022. **9**: p. 967899.
33. Mancina, R.M., et al., *The MBOAT7-TMC4 Variant rs641738 Increases Risk of Nonalcoholic Fatty Liver Disease in Individuals of European Descent.* Gastroenterology, 2016. **150**(5): p. 1219-1230.e6.
34. Mahdessian, H., et al., *TM6SF2 is a regulator of liver fat metabolism influencing triglyceride secretion and hepatic lipid droplet content.* Proc Natl Acad Sci U S A, 2014. **111**(24): p. 8913-8.
35. Lindqvist, D., et al., *Increased plasma levels of circulating cell-free mitochondrial DNA in suicide attempters: associations with HPA-axis hyperactivity.* Transl Psychiatry, 2016. **6**(12): p. e971.
36. Min, H.K., et al., *Metabolic profiling reveals that PNPLA3 induces widespread effects on metabolism beyond triacylglycerol remodeling in Huh-7 hepatoma cells.* Am J Physiol Gastrointest Liver Physiol, 2014. **307**(1): p. G66-76.
37. Lewis, C.M. and E. Vassos, *Polygenic risk scores: from research tools to clinical instruments.* Genome Med, 2020. **12**(1): p. 44.
38. Meroni, M., et al., *MAFLD definition underestimates the risk to develop HCC in genetically predisposed patients.* J Intern Med, 2022. **291**(3): p. 374-376.
39. Sharpe, M.C., et al., *Enhancing Hepatic MBOAT7 Expression in Mice With Nonalcoholic Steatohepatitis.* Gastro Hep Adv, 2023. **2**(4): p. 558-572.
40. Pant, A., et al., *Perturbation of.* Int J Mol Sci, 2021. **22**(18).
41. Shami, G.J., et al., *Three-dimensional ultrastructure of giant mitochondria in human non-alcoholic fatty liver disease.* Sci Rep, 2021. **11**(1): p. 3319.
42. Gong, F., L. Gao, and T. Ding, *IDH2 protects against nonalcoholic steatohepatitis by alleviating dyslipidemia regulated by oxidative stress.* Biochem Biophys Res Commun, 2019. **514**(3): p. 593-600.
43. Galloway, C.A., et al., *Decreasing mitochondrial fission alleviates hepatic steatosis in a murine model of nonalcoholic fatty liver disease.* Am J Physiol Gastrointest Liver Physiol, 2014. **307**(6): p. G632-41.
44. Zhang, Y., et al., *Mitochondrial dysfunction during in vitro hepatocyte steatosis is reversed by omega-3 fatty acid-induced up-regulation of mitofusin 2.* Metabolism, 2011. **60**(6): p. 767-75.
45. Wang, L., et al., *ALCAT1 controls mitochondrial etiology of fatty liver diseases, linking defective mitophagy to steatosis.* Hepatology, 2015. **61**(2): p. 486-96.
46. Boland, M.L., et al., *Nonalcoholic steatohepatitis severity is defined by a failure in compensatory antioxidant capacity in the setting of mitochondrial dysfunction.* World J Gastroenterol, 2018. **24**(16): p. 1748-1765.
47. Zhang, Z., et al., *MFN1-dependent alteration of mitochondrial dynamics drives hepatocellular carcinoma metastasis by glucose metabolic reprogramming.* Br J Cancer, 2020. **122**(2): p. 209-220.
48. Le, T.H., et al., *The zonal distribution of megamitochondria with crystalline inclusions in nonalcoholic steatohepatitis.* Hepatology, 2004. **39**(5): p. 1423-9.
49. Pérez-Carreras, M., et al., *Defective hepatic mitochondrial respiratory chain in patients with nonalcoholic steatohepatitis.* Hepatology, 2003. **38**(4): p. 999-1007.

50. García-Ruiz, I., et al., *Uric acid and anti-TNF antibody improve mitochondrial dysfunction in ob/ob mice.* Hepatology, 2006. **44**(3): p. 581-91.
51. O'Hare, E.A., et al., *TM6SF2 rs58542926 impacts lipid processing in liver and small intestine.* Hepatology, 2017. **65**(5): p. 1526-1542.
52. Ruhanen, H., et al., *Depletion of TM6SF2 disturbs membrane lipid composition and dynamics in HuH7 hepatoma cells.* Biochim Biophys Acta Mol Cell Biol Lipids, 2017. **1862**(7): p. 676-685.
53. Hubens, W.H.G., et al., *Blood biomarkers for assessment of mitochondrial dysfunction: An expert review.* Mitochondrion, 2022. **62**: p. 187-204.
54. Shirakawa, R., et al., *Author Correction: Enhanced mitochondrial oxidative metabolism in peripheral blood mononuclear cells is associated with fatty liver in obese young adults.* Sci Rep, 2024. **14**(1): p. 6786.
55. Lindén, D., et al., *Pnpla3 silencing with antisense oligonucleotides ameliorates nonalcoholic steatohepatitis and fibrosis in Pnpla3 I148M knock-in mice.* Mol Metab, 2019. **22**: p. 49-61.
56. BasuRay, S., et al., *The PNPLA3 variant associated with fatty liver disease (I148M) accumulates on lipid droplets by evading ubiquitylation.* Hepatology, 2017. **66**(4): p. 1111-1124.
57. Weber, M., et al., *Liver CPT1A gene therapy reduces diet-induced hepatic steatosis in mice and highlights potential lipid biomarkers for human NAFLD.* FASEB J, 2020. **34**(9): p. 11816-11837.
58. Vilà, L., et al., *AAV8-mediated Sirt1 gene transfer to the liver prevents high carbohydrate diet-induced nonalcoholic fatty liver disease.* Mol Ther Methods Clin Dev, 2014. **1**: p. 14039.
59. Okochi, O., et al., *Detection of mitochondrial DNA alterations in the serum of hepatocellular carcinoma patients.* Clin Cancer Res, 2002. **8**(9): p. 2875-8.

Supplementary methods

Lentiviral Overexpression

MBOAT7 and TM6SF2 were overexpressed in MBOAT7-/- (MBOAT7+/+) and TM6SF2-/- (TM6SF2+/+) cells and then alone or in combination in MBOAT7-/-TM6SF2-/- clone (MBOAT7+/+TM6SF2-/-, MBOAT7-/-TM6SF2+/+, MBOAT7+/+TM6SF2+/+) through pLenti-C-mGFP-P2A-Puro lentiviral vectors, which were engineered to express a complete ORF fused with a GFP tag. We seeded 3∗104 cells in 24-well plates and they were incubated at 37ºC and 5% CO2 overnight. Multiplicity of infection was set at 2.5 and the number of lentiviral particles for the transduction were calculated according to the manufacturer's instructions (OriGene, Rockville, MD). Lentiviral particles were added to prewarmed cultured media for 24 hours. To introduce MBOAT7-GFP–tagged protein, MBOAT7-/- and MBOAT7-/-TM6SF2-/- cells were transduced with the LENG4 (MBOAT7) Human Tagged ORF Clone Lentiviral Particle (OriGene) containing a molecular sequence that aligns with the MBOAT7 mRNA (gene accession numbers: NM_024298.2 and NP_077274.2). To insert the TM6SF2-GFP, TM6SF2-/- and MBOAT7-/-TM6SF2-/- cells were transfected with TM6SF2 Human Tagged ORF Clone Lentiviral Particle (OriGene) carrying the molecular sequence that aligns with the TM6SF2 mRNA (gene accession numbers: NM_001001524.2 and NP_001001524.2). To embed MBOAT7-GFP and TM6SF2-GFP, MBOAT7-/-TM6SF2-/- cells were co-transduced with both LENG4 (MBOAT7) Human Tagged ORF Clone Lentiviral Particle (OriGene) and TM6SF2 Human Tagged ORF Clone Lentiviral Particle (OriGene). Stable cell lines carrying the WT forms of MBOAT7 and/or TM6SF2 (MBOAT7+/+, TM6SF2+/+, MBOAT7+/+TM6SF2-/-,

MBOAT7-/-TM6SF2+/+, MBOAT7+/+TM6SF2+/+) were selected using the puromycin resistance gene (GE Healthcare Dharmacon, Inc).

Oil Red O (ORO) staining

Cells were plated on a 6-well plate (5 × 105 cells/well) in duplicate and left overnight in Dulbecco's modified Eagle medium (DMEM) containing 10% fetal bovine serum (FBS), 1% L-glutamine, and 1% penicillin/streptomycin. After 24 hours, growth media was removed and cells were kept for 24 hours in quiescent medium, containing 0.5% bovine serum albumin (BSA), 1% L-glutamine, and 1% penicillin/streptomycin. The day after, we performed ORO staining, which is a soluble red powder with high affinity for neutral triacylglycerols (TAGs) and lipids stored in the lipid droplets. Quiescent medium was removed, and the 6-well plates were gently rinsed with 2 mL sterile phosphate-buffered saline 1X. Next, cells were fixed with 4% formalin for 1 hour at room temperature. After fixation, each sample was washed with sterile water and 60% isopropanol was added for 5 minutes. Concurrently, we prepared ORO working solution by mixing 3 parts of ORO stock solution (300 mg of Red Oil powder in 100 mL di-isopropanol 100%) and 2 parts of sterile water, after filtration. ORO working solution (1 mL/well) was added to each sample and left for 40 minutes. Finally, plates were rinsed with tap water, paying attention not to disrupt the monolayer. LD content was visualized in pink-red color. The ORO-positive area was quantified by ImageJ software in 10 random micrographs (magnification, 200X) by calculating the ORO-positive area as a percentage of pixels above the threshold value with respect to the total pixels per area.

Evaluation of Triglycerides and Cholesterol content

A total of 2 x 106 of Cas9, MBOAT7-/-, TM6SF2-/-, MBOAT7-/- TM6SF2-/-, MBOAT7+/+, TM6SF2$^{+/+}$, MBOAT7$^{+/+}$TM6SF2$^{-/-}$, MBOAT7$^{-/-}$TM6SF2$^{+/+}$ and MBOAT7$^{+/+}$TM6SF2$^{+/+}$ cells were culture in DMEM containing 10% FBS, 1% L-glutamine, and 1% penicillin/streptomycin. After 24 hours, growth media was removed and cells were kept for 24 hours in quiescent medium, containing 0.5% bovine serum albumin (BSA), 1% L-glutamine, and 1% penicillin/streptomycin. The day after, cells were lysed in 0.5% Nonidet P-40 (NP-40) lysis buffer and cell lysates were used in quadruplicate to quantify the triglyceride and cholesterol content by exploiting the Triglycerides Colorimetric/Fluorometric Assay Kit and Cholesterol

Colorimetric/Fluorometric Assay Kit, respectively. To measure triglyceride concentration, cells lysates were incubated with lipase for 20 minutes and then with the reaction mix for 30 minutes. The triglycerides will be converted to free fatty acids and glycerol. Glycerol is then oxidized to generate a product which reacts with a probe to generate color (spectrophotometry at λ= 570 nm) and fluorescence (Ex/Em = 535/587 nm). To assess cholesterol amount, cell lysates were incubated with the total cholesterol reaction mix with a specific probe for 60 minutes at 37 ºC generating color (570 nm) or fluorescence (Ex/Em = 538/587 nm).

Gene Expression Analysis

RNA was extracted from cell cultures using TRIzol reagent (Life Technologies–ThermoFisher, Carlsbad, CA). Total RNA (1 μg) was retrotranscribed with the VILO random hexamers synthesis system (Life Technologies–ThermoFisher, Carlsbad, CA). Quantitative real-time PCR was performed by an ABI 7500 fast thermocycler (Life Technologies), using the TaqMan Universal PCR Master Mix (Life Technologies–ThermoFisher, Carlsbad, CA) and TaqMan probes for human GAPDH, MBOAT7, TM6SF2, PGC1α, D-loop and Rnase P. SYBR Green chemistry (Fast SYBR Green Master Mix; Life Technologies–ThermoFisher, Carlsbad, CA) were exploited for the other genes. All reactions were delivered in quadruplicate. Data were normalized to β-actin and G3PDH housekeeping genes and results were expressed as mean and standard error (SE) and graphed as data points. Probes and primers are listed in **Tables S1A** and **S1B**, respectively.

Table S1. **A)** List of TaqMan Probes and **B)** sequence of primers used in Quantitative Real-Time PCR Experiments

A)

PROBES	CATALOG NUMBER
GAPDH	THERMOFISHER HS02786621_G1
MBOAT	THERMOFISHER HS00383302_M1
TM6SF2	THERMOFISHER HS00403495_M1

PPARGC1α (PGC1α)	THERMOFISHER #HS00173304_M1
MT-7S (D-LOOP)	THERMOFISHER #HS02596861_S1
RNASE P	THERMOFISHER #4401631

B)

	FORWARD 5′→3′	**REVERSE 5′→3′**
B-ACTIN	GCTACAGCTTCACCACCACA	AAGGAAGGCTGGAAAAGAGC
MFN1	GAGGTGCTATCTCGGAGACAC	GCCAATCCCACTAGGGAGAAC
MFN2	CACATGGAGCGTTGTACCAG	TTGAGCACCTCCTTAGCAGAC
DRP1	ACCCGGAGACCTCTCATTCT	TGACAACGTTGGGTGAAAAA
FIS1	GATGACATCCGTAAAGGCATCG	AGAAGACGTAATCCCGCTGTT
PPARα	ATGGCATCCAGAACAAGGAG	TCCCGTCTTTGTTCATCACA
COXIII	TGACCCACCAATCACATGC	ATCACATGGCTAGGCCGGAG
ND1	CCCTAAAACCCGCCACATCT	GAGCGATGGTGAGAGCTAAGGT
DUSP1	CCTGACAGCGCGGAATCT	GATTTCCACCGGGCCAG
MCL1	CCAAGAAAGCTGCATCGAACCAT	CAGCACATTCCTGATGCCACCT
BAX	TTTGCTTCAGGGTTTCATCC	TCCTCTGCAGCTCCATGTTA

Western Blot Analysis

Total protein lysates were extracted from cell cultures, using RIPA buffer containing 1 mmol/L Na-orthovanadate, 200 mmol/L phenylmethyl sulfonyl fluoride, and 0.02 μg/μL aprotinin. Samples were pooled prior to electrophoretic separation, and all reactions were performed in duplicate. Then, equal amounts of proteins (50 μg) were separated by SDS-PAGE, transferred

electrophoretically to nitrocellulose membrane (BioRad, Hercules, CA, USA), and incubated with specific antibodies overnight. At least, three independent lots of freshly extracted proteins were used for experiments. The antibodies and concentration used are listed in **TableS2**.

Table S2. List of Antibodies and Relative Dilutions Used in Western Blot (WB) and Immunocytochemistry (ICC) Experiments

ANTIBODY	CATALOG NUMBER
Vinculin (1:1000 WB)	ABCAM #AB73412
MBOAT7 (1:1000 WB)	SIGMA-ALDRICH AV49811
TM6SF2 (1:1000 WB)	THERMOFISHER PA5-69304
PGC1α (1:1000 WB; 1:200 ICC)	NOVUS BIOLOGICALS NBP1-04676
MFN1 (1:1000 WB; 1:200 ICC)	ABCAM #AB126575
MFN2 (1:200 ICC)	ABCAM #AB56889
OPA1 (1:1000 WB; 1:200 ICC)	ACAM #AB119685
DRP1 (1:1000 WB; 1:200 ICC)	ABCAM #AB56788
PARKIN (1:1000 WB; 1:200 ICC)	CELL SIGNALING #4211
PINK (1:1000 WB)	CELL SIGNALING #6946
BNIP3-L (1:1000 WB)	CELL SIGNALING #44060
BNIP3 (1:1000 WB)	CELL SIGNALING #12396
LC3 (1:1000 WB)	CELL SIGNALING #3868
PHOSPHO-UBIQUITIN (1:1000 WB)	CELL SIGNALING #62802
OXPHOS (1:1000 WB)	ABCAM #AB110411
COXI	ABCAM AB110216
SDHA	ABCAM AB110216

Immunocytochemistry (ICC)

A total of 1×10^5 cells were seeded on coverslips lodged in a 6-well plate in duplicate and kept overnight in DMEM containing 10% FBS, 1% L-glutamine, and 1% penicillin/streptomycin.

After 24 hours, growth media was removed and cells were kept for 24 hours in quiescent medium, containing 0.5% bovine serum albumin (BSA), 1% L-glutamine, and 1% penicillin/streptomycin. Next, hepatocytes were fixed in 4% formalin for 10 minutes and permeabilized in 0.3% Triton X-100 (Sigma-Aldrich, St Louis, MO). Cells were incubated in 5% BSA for 30 minutes and with anti- primary antibody (**Table S2**) overnight at 4°C. Then, each sample was incubated with anti-rabbit/mouse horseradish-peroxidase–conjugated antibody, and 3,3′-diaminobenzidine was provided as chromogen. Nucleus were counterstained with hematoxylin. Finally, samples were mounted with a drop of aqueous VectaMount AQ Mounting Medium (Maravai LifeSciences, Inc, San Diego, CA).

Evaluation of Mitochondrial Complex I activity

A total of 5mg/ml of NAFLD patients liver biopsies and PBMCs homogenate in MAS buffer was loaded in a 96-well plate in quadruplicate. The mitochondrial complex I enzyme activity was measured through a colorimetric assay at 450 nm at 20 second-1min intervals for up to 30 minutes with shake between readings at room temperature by using an Assay solution (Abcam, Cambridge, UK).

Evaluation of Mitochondrial Complex III activity

A total of 3 x 10^6 of cells were culture in DMEM containing 10% FBS, 1% L-glutamine, and 1% penicillin/streptomycin. After 24 hours, growth media was removed and cells were kept for 24 hours in quiescent medium, containing 0.5% bovine serum albumin (BSA), 1% L-glutamine, and 1% penicillin/streptomycin. The day after, mitochondria were isolated from cell lysates by exploiting a Mitochondria Isolation Kit for Cultured Cells (Abcam, Cambridge, UK). The mitochondria were resuspended in RIPA buffer and 1.5 to 10 μg was seeded in a 96-well plate in quadruplicate. Additionally, 15 μg of NAFLD patients liver biopsies and PBMCs homogenate in MAS buffer were loaded in a 96-well plate in quadruplicate. The mitochondrial complex III activity was measured through a colorimetric assay at 550 nm at 30 second intervals for up to 10 minutes at room temperature by using a Sample Mix alone or in combination with Antimycin A, specific inhibitor of the mitochondrial complex III (Abcam, Cambridge, UK).

Evaluation of Mitochondrial Complex IV activity

Mitobiogenesis In-Cell ELISA Kit Abcam (Cambridge, UK) exploits a quantitative immunocytochemistry (ICC) to measure subunit I of mitochondrial COXI (Complex IV) and nuclear DNA (nDNA)-encoded succinate dehydrogenase complex flavoprotein subunit A (SDHA) protein levels in live cells. Briefly, cells are seeded in a 96-well plate ($3x10^5$/well) in quadruplicate, fixed with 4% paraformaldehyde and permeabilized through 1X Triton-X 100. Targets of interest were detected with highly specific, well-characterized cocktail of monoclonal antibodies, which were incubated overnight at 4°C. Then, AP-labelled and HRP-labeled secondary antibodies were used to generate a colorimetric reaction that could be measured at 405 and 600 nm, respectively.

Evaluation of Mitochondrial Complex V activity

A total of 3×10^6 of cells were culture in DMEM containing 10% FBS, 1% L-glutamine, and 1% penicillin/streptomycin. After 24 hours, growth media was removed and cells were kept for 24 hours in quiescent medium, containing 0.5% bovine serum albumin (BSA), 1% L-glutamine, and 1% penicillin/streptomycin. The day after, mitochondria were isolated from cell lysates by exploiting a Mitochondria Isolation Kit for Cultured Cells (Abcam, Cambridge, UK) and resuspended in RIPA buffer. The ATP Synthase Enzyme Activity Microplate Assay Kit (Abcam, Cambridge, UK) exploits a quantitative ELISA assay to measure the mitochondrial Complex V by using Capture antibodies that are pre-coated in the wells of premium Nunc MaxiSorp™ modular microplates. 10 μg/50 μL of extracted mitochondria and 15 μg of NAFLD patients liver biopsies and PBMCs homogenate in MAS buffer were added in quadruplicate on the plate and incubated for 3 hours at room temperature. Then, empty the wells and incubate the Lipid Mix for 45 minutes at room temperature. Finally, the Reagent Mix was added to generate a colorimetric reaction that could be measured at 340 nm at 30°C for 60-120 minutes.

Evaluation of Citrate Synthase activity

A total of 3 x 106 of cells were culture in DMEM containing 10% FBS, 1% L-glutamine, and 1% penicillin/streptomycin. After 24 hours, growth media was removed and cells were kept for

24 hours in quiescent medium, containing 0.5% bovine serum albumin (BSA), 1% L-glutamine, and 1% penicillin/streptomycin. The day after, mitochondria were isolated from cell lysates by exploiting a Mitochondria Isolation Kit for Cultured Cells (Abcam, Cambridge, UK). The mitochondria were resuspended in RIPA buffer and 1-50 μL were added in a 96 well plate as well as 5 μl of NAFLD patients liver biopsies and PBMCs homogenate in MAS buffer in quadruplicate for the Citrate Synthase Assay Kit (Abcam, Cambridge, UK). The Reaction Mix was used to measure absorbance at 412 nm at 25°C for 20-40 minutes.

Evaluation of Lactate Dehydrogenase enzymatic activity

A total of 3 x 10^6 of cells were culture in DMEM containing 10% FBS, 1% L-glutamine, and 1% penicillin/streptomycin. After 24 hours, growth media was removed and cells were kept for 24 hours in quiescent medium, containing 0.5% bovine serum albumin (BSA), 1% L-glutamine, and 1% penicillin/streptomycin. The day after, it was performed the Lactate Dehydrogenase (LDH) Assay Kit (Abcam, Cambridge, UK) to measure the LDH enzymatic activity. Cells were homogenate with Assay Buffer in ice, centrifuge at 4°C at 10,000 x g for 15 minutes and collect the supernatant. 50 μL of cell lysates in quadruplicate were added in 96 well and incubated with a Reaction Mix containing the LDH assay buffer and LDH substrate mix to measure the absorbance at 450 nm for 30-60 minutes at 37°C.

Evaluation of Lactate Dehydrogenase production

A total of 3 x 10^6 of cells were culture in DMEM containing 10% FBS, 1% L-glutamine, and 1% penicillin/streptomycin. After 24 hours, growth media was removed and cells were kept for 24 hours in quiescent medium, containing 0.5% bovine serum albumin (BSA), 1% L-glutamine, and 1% penicillin/streptomycin. The day after, the medium was collected and concentrated with Vivaspin® 2 Centrifugal Concentrator (Sartorius, Göttingen, Germany) to measure the LDH activity by Lactate Dehydrogenase (LDH) Assay Kit (Abcam, Cambridge, UK) which exploits the conversion of lactate into pyruvate and NADH. 50 μL of concentrated culture media was plated in quadruplicate in 96 well and then, the reaction mix containing

the LDH assay buffer, the PicoProbe and LDH substrate mix was added to measure the fluorescence reaction at Ex/Em 535/587 nm for 10-30 minutes at 37°C.

Mito Stress Seahorse Assay

The Agilent Seahorse XF Cell Mito Stress Test measures parameters of mitochondrial function by directly quantifying the oxygen consumption rate (OCR) of cells on the Seahorse XFe and XF Extracellular Flux Analyzers. The assay uses the built-in injection ports on XF sensor cartridges to add modulators of respiration into cell well during the test that are Oligomycin, Carbonyl cyanide-4 (trifluoromethoxy) phenylhydrazone (FCCP), Rotenone, and Antimycin. $5x10^4$ cells in quadruplicate were plated on a Seahorse XF24-well microplate in DMEM containing 10% FBS, 1% L-glutamine, and 1% penicillin/streptomycin. After 24 hours, the growth media was replaced by the assay medium, supplemented with glucose, pyruvate, and glutamine, and cells were incubated at 37°C for 60 minutes. Then, Seahorse XF24-well microplate was adapted on the pre-warmed XF sensor cartridges congaing the Oligomycin, FCCP, Rotenone and Antimycin drugs and the OCR was measured through XFe24 analyzer, with 3 baseline measurements recorded before and after adding several drugs (1.5 μM Oligomycin, 0.5 μM FCCP and 0.5 μM Rotenone + Antimycin).

Glycolytic Seahorse Assay

The Agilent Seahorse XF Glycolysis Stress Test is the standard assay for measuring glycolytic function in cells by directly measuring the extracellular acidification rate (ECAR) and assesses the key parameters of glycolytic flux: Glycolysis, Glycolytic Capacity, Glycolytic Reserve, as well as non-glycolytic acidification. The assay uses the built-in injection ports on XF sensor cartridges to add modulators of glycolysis into cell well during the test that are Oligomycin and 2-deoxy-glucose (2-DG), a glucose analog. $5x10^4$ cells in quadruplicate were plated on a Seahorse XF24-well microplate in DMEM containing 10% FBS, 1% L-glutamine, and 1% penicillin/streptomycin. After 24 hours, the growth media was replaced by the glycolysis stress test medium without glucose or pyruvate and cells were incubated at 37°C for 60 minutes. Then, Seahorse XF24-well microplate was adapted on the pre-warmed XF sensor cartridges congaing oligomycin and 2-DG to measure ECAR through XFe24 analyzer, with 3

baseline measurements recorded before and after adding several drugs (5 μM Oligomycin and 500 mM 2-DG).

Evaluation of ROS/RNS production

The Cellular ROS/RNS Detection Assay Kit (Abcam, Cambridge, UK) is designed to directly monitor real time reactive oxygen and/or nitrogen species (ROS/RNS) production in live cells using fluorescence microscopy. Cells are seeded in a 96-well plate ($3x10^5$/well) in quadruplicate in DMEM containing 10% FBS, 1% L-glutamine, and 1% penicillin/streptomycin to ensure 50- 70% confluency on the day of the experiment. Then, growth media was removed, and cells were kept for 24 hours in quiescent medium, containing 0.5% bovine serum albumin (BSA), 1% L-glutamine, and 1% penicillin/streptomycin. The day after, cells and 10 μg of NAFLD patients liver biopsies and PBMCs homogenate in MAS buffer were loaded with the ROS/RNS 3-Plex Detection Mix containing Oxidative Stress Detection Reagent, Superoxide Detection Reagent and NO Detection Reagent for 2 hours. For the last 30 minutes, cells were treated with the NO Inducer (L-Arginine) and the ROS Inducer (Pyocyanin). After rinsing the cells, they could be observed under fluorescent/confocal microscope or it could detect oxidative stress (ROS) and superoxide (RNS) at Ex/Em 490/525nm and 550/620nm, respectively.

Evaluation of apurinic/apyrimidinic (AP) sites

A total of 3×10^6 of cells were culture in DMEM containing 10% FBS, 1% L-glutamine, and 1% penicillin/streptomycin. After 24 hours, growth media was removed and cells were kept for 24 hours in quiescent medium, containing 0.5% bovine serum albumin (BSA), 1% L-glutamine, and 1% penicillin/streptomycin. The day after, genomic DNA was extracted from cell lysates through QIAmp DNA Mini Kit (Manchester, UK). Cells lysates were resuspended in a Protease solution and incubated 56°C for 10 minutes to disruptprotein-DNAinteractions. Total DNA was trapped onto the QIAamp silica membrane, while contaminants were removed in the flowthrough. Subsequently, DNA was eluted in water and its concentration and quality were assessed by Nanodrop 1000 microvolume 42 spectrophotometer (ThermoFisher Scientific, U.S.A.). 100 μg/mL of purified genomic DNA was used for the DNA

damage – AP sites – Assay Kit (Abcam, Cambridge, UK) to detect aldehyde site (AP sites) at 450 nm.

Evaluation of Malondialdehyde production

A total of 3 x 10^6 of cells were culture in DMEM containing 10% FBS, 1% L-glutamine, and 1% penicillin/streptomycin. After 24 hours, growth media was removed and cells were kept for 24 hours in quiescent medium, containing 0.5% bovine serum albumin (BSA), 1% L-glutamine, and 1% penicillin/streptomycin. The day after, cells were lysed in 0.5% Nonidet P-40 (NP-40) lysis buffer and cell lysates were used in quadruplicate to perform the Lipid Peroxidation (MDA) Assay Kit (Abcam, Cambridge, UK). Cell lysates were incubated at room temperature for 30-60 minutes with the MDA color reagent solution and then measure the absorbance at 695-700 nm.

Wound Healing Assay

Cells were plated on 6-well plate (8 × 10^5/well) and incubated with DMEM containing 10% FBS, 1% L-glutamine, and 1% penicillin/streptomycin. A fine scratch was introduced using a sterile pipette tip in a monolayer of cells at approximately 90% confluency. The wounds were photographed (objective, 100×) at 24 and 48 hours. Each experiment was performed in triplicate.

Cell Proliferation Assay

2.5 x 10^2 cells/well were seeded in a 96-well plate in quadruplicate and incubated in DMEM containing 10% FBS, 1% L-glutamine, and 1% penicillin/streptomycin overnight. Cell proliferation was measured at baseline using the CellTiter96-Aqueous One Solution Cell Proliferation Assay (MTS:3-(4,5-dimethylthiazol-2-yl)-5-(3-carboxymethoxyphenyl)-2-(4-sulfophenyl)-2H-tetrazolium)) kit (Promega Corporation, Fitchburg, WI). Fresh growth media was provided for 24-48-72 h and 1 week. MTS reagent (20 µL/well) was added to the cells followed by incubation for 4 hours in a 5% CO2 humidified incubator at 37°C, and the absorbance was measured at 490 nm, at 0, 24, 48, and 74 hours, and after 1 week. At least 3 independent experiments were performed.

Invasion Assay

The invasion assay[17] exploits the transwell insert membrane coated with Collagen (3 mg/mL) above which 25 x 10^3 cells were plated in duplicate in DMEM containing 10% FBS, 1% L-glutamine, and 1% penicillin/streptomycin. The underside of the transwell was filled with culture media. After 24 hours, growth media was removed and cells were kept for 24 hours in quiescent medium, containing 0.5% bovine serum albumin (BSA), 1% L-glutamine, and 1% penicillin/streptomycin. After 24 and 48 hours, cells were fixed in 4% formalin for 10 minutes. The transwell membrane containing the fixed cells was cut and mounted with a drop of aqueous VectaMount AQ Mounting Medium on a cover slide. Cells were photographed (objective, 100×) at 24 and 48 hours. Each experiment was performed in triplicate.

Supplementary results

The lentiviral overexpression of MBOAT7 and/or TM6SF2 wild-type genes in CRISPR-Cas9 knock-out models

MBOAT7 and TM6SF2 deficiency in HepG2 cells led to mitochondrial aberrances. Therefore, to explore whether their recovery could have an impact on mitochondrial number, morphology and function we leveraged a lentiviral transfection in MBOAT7$^{-/-}$, TM6SF2$^{-/-}$ and MBOAT7$^{-/-}$TM6SF2$^{-/-}$ cells by using pLenti-C-mGFP-P2A-Puro lentiviral vectors containing the puromycin selection aiming to obtain stable cell lines (MBOAT7$^{+/+}$, TM6SF2$^{+/+}$, MBOAT7$^{+/+}$TM6SF2$^{-/-}$, MBOAT7$^{-/-}$TM6SF2$^{+/+}$, MBOAT7$^{+/+}$TM6SF2$^{+/+}$). The vector deigns embraces a GFP tag fused with an ORF targeting the protein which should be upregulated (OriGene Technologies, Inc., PS100093). The messenger RNA (mRNA) and protein levels of MBOAT7 and TM6SF2 significantly increased in MBOAT7$^{-/-}$ (**Figure S1A-B**) and TM6SF2$^{-/-}$ (**Figure S1C-D**) cells alone or in combination in MBOAT7$^{-/-}$TM6SF2$^{-/-}$ ones (**Figure S1E-F**), thus restoring the CRISPR-Cas9-driven deletion which mimics the human protein loss-of-

functions (adjusted **p<0.01 *vs* MBOAT7$^{-/-}$, TM6SF2$^{-/-}$, MBOAT7$^{-/-}$TM6SF2$^{-/-}$; adjusted *p<0.05 *vs* MBOAT7$^{-/-}$).

Since MBOAT7 and TM6SF2 natural functional role allows to lipid assembly, metabolism, and transport, we evaluated the intracellular LDs in KO and overexpressed models by exploiting the ORO staining. Lipid accumulation was significantly lower in MBOAT7$^{+/+}$ and TM6SF2$^{+/+}$ cells compared to MBOAT7$^{-/-}$ and TM6SF2$^{-/-}$, respectively, showing a similar Cas9 phenotype. Despite both MBOA T7$^{+/+}$TM6SF2$^{-/-}$ and MBOAT7$^{-/-}$TM6SF2$^{+/+}$ models exhibited a strong lipid reduction than MBOAT7$^{-/-}$TM6SF2$^{-/-}$ clone, deletion of MBOAT7 or TM6SF2 alone depicts a mirror effect on LDs size. Indeed, MBOAT7 KO in MBOAT7$^{-/-}$TM6SF2$^{+/+}$ clone led to larger LDs size due to their enrichment in saturated/monounsaturated TAG [30]. Otherwise, TM6SF2 KO in MBOAT7$^{+/+}$TM6SF2$^{-/-}$ cell line promotes the assembly of small LDs by overexpressing saturated diacylglycerols (DAGs) [27]. The greatest reduction in intracellular fat was detected in MBOAT7$^{+/+}$TM6SF2$^{+/+}$ model, thus suggesting that the restore of both MBOAT7 and TM6SF2 proteins rather than one could protect against steatosis (**Figure S1G**). According to the qualitative results, the measurement of ORO-positive area (**Figure S1H**) alongside intracellular triglycerides (**Figure S1I**) and cholesterol (**Figure S1J**) content significantly decreased in all the overexpressed cells compared to the KO ones (adjusted **p<0.01 *vs* Cas9, MBOAT7$^{-/-}$, TM6SF2$^{-/-}$, MBOAT7$^{-/-}$TM6SF2$^{-/-}$).

Proliferation and invasiveness drop after the overexpression of MBOAT7 and/or TM6SF2 wild-type genes

To investigate the involvement of MBOAT7 and TM6SF2 loss-of-functions in the malignant transformation and to deepen how their WT overexpression could attenuate the carcinogenesis, we examined cells proliferation and invasiveness. The scratch test revealed that at 48 hours the wound healing was improved in MBOAT7$^{-/-}$, TM6SF2$^{-/-}$ and completely patched up in MBOAT7$^{-/-}$ TM6SF2$^{-/-}$cell lines. Conversely, all overexpressed cells showed a slight proliferative phenotype (**Figure S4A**). In keeping with these results, the MTS assay (**Figure S4B**) highlighted the increased proliferation rate from 48 hours peaking at 1 week in MBOAT7$^{-/-}$, TM6SF2$^{-/-}$ and MBOAT7$^{-/-}$ TM6SF2$^{-/-}$ models compared to their overexpressed ones, exhibiting the higher growth rate in MBOAT7$^{-/-}$ TM6SF2$^{-/-}$ clone detectable at 48 and

even more at 72 hours (adjusted *p<0.05, **p<0.01 *vs* Cas9, MBOAT7$^{-/-}$, TM6SF2$^{-/-}$, MBOAT7$^{-/-}$ TM6SF2$^{-/-}$). Inversely, the WT upregulation of *MBOAT7* and *TM6SF2* alone and in combination significantly reduced the growth capacity from 24 hours up to 1 week. According to these data, mRNA levels of *Dual Specificity Phosphatase 1* (*DUSP1*) (**Figure S4C**) and *Induced Myeloid Leukemia Cell Differentiation Protein* (*MCL1*) (**Figure S4D**), genes acting in proliferation and anti-apoptotic processes, respectively, augmented in MBOAT7$^{-/-}$, TM6SF2$^{-/-}$ and MBOAT7$^{-/-}$ TM6SF2$^{-/-}$ cell lines whereas decreased after *MBOAT7* and/or *TM6SF2* WT overexpression, (adjusted *p<0.05 vs MBOAT7$^{-/-}$ TM6SF2$^{-/-}$; **p<0.01 *vs* Cas9, MBOAT7$^{-/-}$, TM6SF2$^{-/-}$, MBOAT7$^{-/-}$TM6SF2$^{-/-}$). Otherwise, the expression of *Bcl-2-associated X protein* (*BAX*) (**Figure S4E**), a pro-apoptotic regulator, was downregulated after the deletion of *MBOAT7* and/or *TM6SF2* genes while strongly rose beyond their WT overexpression (**p<0.01 *vs* MBOAT7$^{-/-}$, TM6SF2$^{-/-}$, MBOAT7$^{-/-}$TM6SF2$^{-/-}$). Finally, we investigated cell migration by exploiting cells aptitude to pass across transwell insert membrane covered by collagen (**Figure S4F**). At 48 hours the number of migrated cells increased in MBOAT7$^{-/-}$ cells and even more in TM6SF2$^{-/-}$ and MBOAT7$^{-/-}$ TM6SF2$^{-/-}$ models showing high cells quantity already at 24 hours. In comparison, the WT overexpression of *MBOAT7* and *TM6SF2* attenuated the invasiveness at both 24 and 48 hours displaying the hugely effect in MBOAT7$^{+/+}$ TM6SF2$^{+/+}$ clone (**p<0.01 *vs* MBOAT7$^{-/-}$, TM6SF2$^{-/-}$, MBOAT7$^{-/-}$ TM6SF2$^{-/-}$). Therefore, the restore of MBOAT7 and TM6SF2 WT functions in KO models could ameliorate the tumorigenic phenotype by reducing the proliferation capacity and invasiveness.

Table S3. At generalized linear model adjusted for age, sex, body mass index (BMI) and impaired fasting glucose/type 2 diabetes (IFG/T2D), the co-presence of the PNPLA3, MBOAT7 and TM6SF2 variants (NRV=3) in the liver biopsies of the Discovery cohort was associated with: ROS/RNS production (P =0.0011, β = 267.58 % CI, 110.84 to 4242.31); H_2O_2 release (P=0.05, β =4.07, 95% CI, -0.06 to 8.22); low citrate synthase activity (P<0.0001, β = -0.02 % CI, -0.03 to -0.01); low mitochondrial complex I activity (P=0.0004, β = -0.037 % CI, -0.058 to -0.017); low mitochondrial complex III activity (P=0.009, β = -0.011 % CI, -0.02 to -0.003); low ATP synthase (mitochondrial complex V) activity (P <0.0001, β = -0.046 % CI, -0.058 to -0.035). Values are reported as mean±SD, number (%) or median {IQR}, as appropriate. BMI: body mass index;

IFG/T2D: impaired fasted glucose/ type 2 diabetes; NRV: number of risk variants; β: beta coefficients; CI: confidence interval. p<0.05 was considered statistically significant.

Liver biopsies	ROS/RNS		H_2O_2	
	β {95% CI}	**P value**	**β {95% CI}**	**P value**
Age, Years	-3.30{-12.08-5.47}	0.45	-0.12{-0.35-0.11}	0.30
Sex, M	-136.80 {-258.15- -15.45}	**0.027**	-4.38 {-7.59- -1.17}	0.08
BMI, Kg/m2	4.99 {-23.71-33.70}	0.72	0.42 {-0.34-1.17}	0.27
IFG/T2D, yes	47.21 {-79.25-173.68}	0.45	-0.24 {-3.58-3.10}	0.88
NRV=3	267.58 {110.84-4242.31}	**0.0011**	4.07 {-0.06-8.22}	**0.05**
	Citrate synthase		**Mitochondrial complex I**	
Age, Years	0.0003 {-0.0002-0.0009}	0.26	0.0014 {0.0002-0.002}	**0.015**
Sex, M	0.001 {-0.006- -0.009}	0.72	-0.012 {-0.028-0.003}	0.11
BMI, Kg/m2	0.0013 {-0.0005-0.003}	0.15	0.003 {-0.0003-0.0037	0.07
IFG/T2D, yes	-0.007 {-0.15- -0.0008}	0.07	0.002 {-0.014-0.018}	0.77
NRV=3	-0.01 {0.0018- -0.02}	**0.02**	-0.037 {-0.058- -0.017}	**0.0004**
	Mitochondrial complex III		**Mitochondrial complex V**	
Age, Years	-0.0006{-0.0004-0.0005}	0.08	-0.0008{-0.0015-0.0001}	**0.017**
Sex, M	0.004 {-0.002-0.01}	0.17	-0.003 {-0.12-0.0005}	0.47
BMI, Kg/m2	0.0003 {-0.0012-0.002}	0.62	0.0013 {-0.0007-0.003}	0.20
IFG/T2D, yes	0.005 {-0.001-0.013}	0.10	0.013 {0.004-0.022}	**0.005**
NRV=3	-0.011 {-0.02- -0.003}	**0.009**	-0.046 {-0.058- -0.035}	**<0.0001**

Table S4. At generalized linear model adjusted for age, sex, body mass index (BMI) and impaired fasting glucose/type 2 diabetes (IFG/T2D), the co-presence of the PNPLA3, MBOAT7 and TM6SF2 variants (NRV=3) in the PBMCs of the Discovery cohort was associated with: low citrate synthase activity (P=0.02, β = -0.01 % CI, 0.0018 to -0.02); low mitochondrial complex I activity (P=0.02, β = -0.02 % CI, 0.048 to -0.003); low mitochondrial complex III activity (P<0.0001, β = -0.02 % CI, -0.03 to -0.01); low ATP synthase (mitochondrial complex V) activity (P=0.02, β = -0.01 % CI, 0.0018 to -0.022). Values are reported as mean±SD, number (%) or median {IQR}, as appropriate. BMI: body mass index; IFG/T2D: impaired fasted glucose/ type

2 diabetes; NRV: number of risk variants; β: beta coefficients; CI: confidence interval. $p<0.05$ was considered statistically significant.

PBMCs	ROS/RNS		H_2O_2	
	β {95% CI}	**P value**	**β {95% CI}**	**P value**
Age, Years	-2.97{-12.63-6.69}	0.54	0.018 {-0.19-0.22}	0.85
Sex, M	47.44 {-77.04-171.92}	0.44	0.56 {-2.15-3.28}	0.67
BMI, Kg/m2	49.86 {20.80-78.91}	**0.0011**	1.11 {0.47-1.74}	**0.0009**
IFG/T2D, yes	-31.61 {-162.63-99.40}	0.63	-1.52 {-4.38-1.33}	0.28
NRV=3	1.85 {-157.29-161.01}	0.98	0.50 {-2.98-3.96}	0.77
	Citrate synthase		**Mitochondrial complex I**	
Age, Years	0.0009 {0.0003-0.001}	**0.001**	0.0006 {-0.0007-0.002}	0.36
Sex, M	-0.004 {-0.011-0.003}	0.25	-0.0019 {-0.019-0.016}	0.82
BMI, Kg/m2	0.0011 {-0.0006-0.002}	0.22	0.0052 {0.001-0.009}	**0.013**
IFG/T2D, yes	-0.0038 {-0.011-0.004}	0.33	-0.011 {-0.03-0.007}	0.24
NRV=3	-0.02 {-0.03- -0.01}	**<0.0001**	-0.02 {-0.048- -0.003}	**0.02**
	Mitochondrial complex III		**Mitochondrial complex V**	
Age, Years	-0.0006 {-0.0004-0.0003}	0.74	0.0003{-0.0002-0.0009}	0.0003
Sex, M	-0.007 {-0.12- -0.001}	**0.009**	0.001 {-0.006-0.009}	0.72
BMI, Kg/m2	0.0003 {-0.0016-0.0008}	0.52	0.0013 {-0.0005-0.003}	0.15
IFG/T2D, yes	0.001 {-0.004-0.006}	0.68	-0.007 {-0.015-0.0008}	0.07
NRV=3	-0.02 {-0.03- -0.01}	**<0.0001**	-0.01 {0.0018-0.022}	**0.02**

Supplementary legend figures

Figure S1. ***MBOAT7 and/or TM6SF2 WT overexpression improves lipid overload due to their silencing.*** **A-C-E)** The expression of *MBOAT7* and *TM6SF2* was evaluated by reverse-transcription quantitative PCR and normalized to the β-actin housekeeping gene. **B-D-F)** Protein levels of MBOAT7 and TM6SF2 tagged with GFP (MBOAT7-GFP and TM6SF2-GFP) were assessed by Western blot and normalized to the vinculin housekeeping gene. **G**) LDs accumulation was assessed by ORO staining (magnification, 630×). **H)** ORO positive (+ve) areas were quantified by ImageJ in 6 random nonoverlapping micrographs per condition by calculating the percentage of pixels above the threshold value in respect to total pixels per area. **I)** The intracellular triglycerides amount was measured by exploiting the Triglycerides Colorimetric/Fluorometric Assay. **J)** Total cholesterol was measured in cell lysates by using the Cholesterol Colorimetric/Fluorometric Assay Kit. At least 3 independent experiments were conducted. For bar graphs, data are expressed as means and SE. Adjusted $*P < .05$ and $**P < .01$.

Figure S2. MBOAT7 and/or TM6SF2 WT overexpression rebalances the mitochondrial lifecycle and turnover. **A-E)** The mRNA levels of *PGC1*a, *Mfn1*, *Mfn2*, *Drp1* and *Fis1* was evaluated by reverse-transcription quantitative PCR and normalized to the β-actin housekeeping gene. **F-I)** Cytoplasmatic and nuclear localization of Mfn1, Mfn2, Opa1 and Drp1 were represented by Immunocytochemistry pictures. At least 3 independent experiments were conducted. For bar graphs, data are expressed as means and SE. Adjusted $*P < .05$ and $**P < .01$

Figure S3. MBOAT7 and/or TM6SF2 WT overexpression in knock-out models restore the mitochondrial functions. **A)** The complex III enzymatic activity was measured through a colorimetric assay in isolated mitochondria. **B)** the MTCO1 (mtDNA– encoded subunit of the complex IV) activity was measured by Mitobiogenesis In-Cell ELISA Kit in isolated mitochondria from cell lysates. **C)** The ATP5A (mtDNA–encoded subunit of the complex V) activity was quantified by ATP Synthase Enzyme Activity Microplate Assay Kit in isolated mitochondria from cell lysates. **D)** The citrate synthase activity was assessed through the Citrate Synthase Assay Kit in isolated mitochondria from cell lysates. At least 3 independent experiments were conducted. For bar graphs, data are expressed as means and SE. Adjusted $*P < .05$ and $**P < .01$.

Fig S4. ***MBOAT7 and/or TM6SF2 WT restore in knock-out cells attenuates the tumorigenic phenotype.*** **A)** Representative images of wound healing assay were acquired at 0, 24 and 48 hours (magnification, 100×). The dotted lines indicate the scratch width. **B)** The proliferation rate was examined through MTS assay for 0, 24, 48, 72 hours and 1 week (λ = 490 nm). **C-D-E)** The expression of *DUSP1, MCL1* and *BAX* was evaluated by reverse-transcription quantitative PCR and normalized to the β-actin housekeeping gene. **F)** Representative images of invasiveness assay were acquired at 24 and 48 hours (magnification, 100×). The total number of cells were quantified by ImageJ in 10 random nonoverlapping micrographs per condition. At least 3 independent experiments were conducted. For bar graphs, data are expressed as means and SE. Adjusted $*P < .05$ and $**P < .01$.

Figure 1

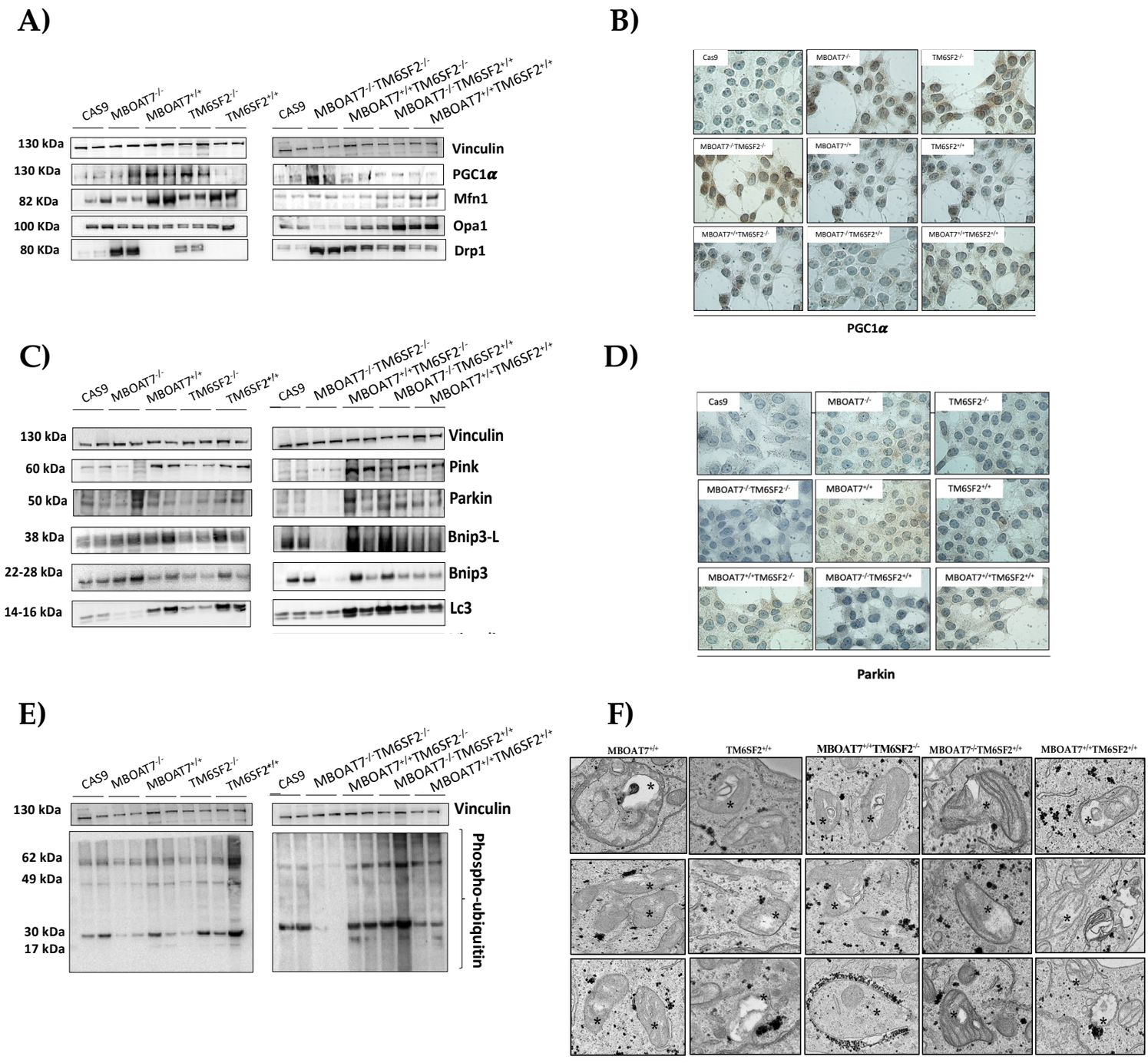
A)
CAS9
MBOAT7-/-
MBOAT7+/+
TM6SF2-/-
TM6SF2+/+
CAS9
MBOAT7-/-TM6SF2-/-
MBOAT7+/+TM6SF2-/-
MBOAT7-/-TM6SF2+/+
MBOAT7+/+TM6SF2+/+
130 kDa
130 KDa
82 KDa
100 KDa
80 KDa
Vinculin
PGC1α
Mfn1
Opa1
Drp1
B)
Cas9
MBOAT7-/-
TM6SF2-/-
MBOAT7-/-TM6SF2-/-
MBOAT7+/+
TM6SF2+/+
MBOAT7+/+TM6SF2-/-
MBOAT7-/-TM6SF2+/+
MBOAT7+/+TM6SF2+/+
PGC1α
C)
CAS9
MBOAT7-/-
MBOAT7+/+
TM6SF2-/-
TM6SF2+/+
CAS9
MBOAT7-/-TM6SF2-/-
MBOAT7+/+TM6SF2-/-
MBOAT7-/-TM6SF2+/+
MBOAT7+/+TM6SF2+/+
130 kDa
60 kDa
50 kDa
38 kDa
22-28 kDa
14-16 kDa
Vinculin
Pink
Parkin
Bnip3-L
Bnip3
Lc3
D)
Cas9
MBOAT7-/-
TM6SF2-/-
MBOAT7-/-TM6SF2-/-
MBOAT7+/+
TM6SF2+/+
MBOAT7+/+TM6SF2-/-
MBOAT7-/-TM6SF2+/+
MBOAT7+/+TM6SF2+/+
Parkin
E)
CAS9
MBOAT7-/-
MBOAT7+/+
TM6SF2-/-
TM6SF2+/+
CAS9
MBOAT7-/-TM6SF2-/-
MBOAT7+/+TM6SF2-/-
MBOAT7-/-TM6SF2+/+
MBOAT7+/+TM6SF2+/+
130 kDa
62 kDa
49 kDa
30 kDa
17 kDa
Vinculin
Phospho-ubiquitin
F)
MBOAT7+/+
TM6SF2+/+
MBOAT7+/+TM6SF2-/-
MBOAT7-/-TM6SF2+/+
MBOAT7+/+TM6SF2+/+

Figure 2

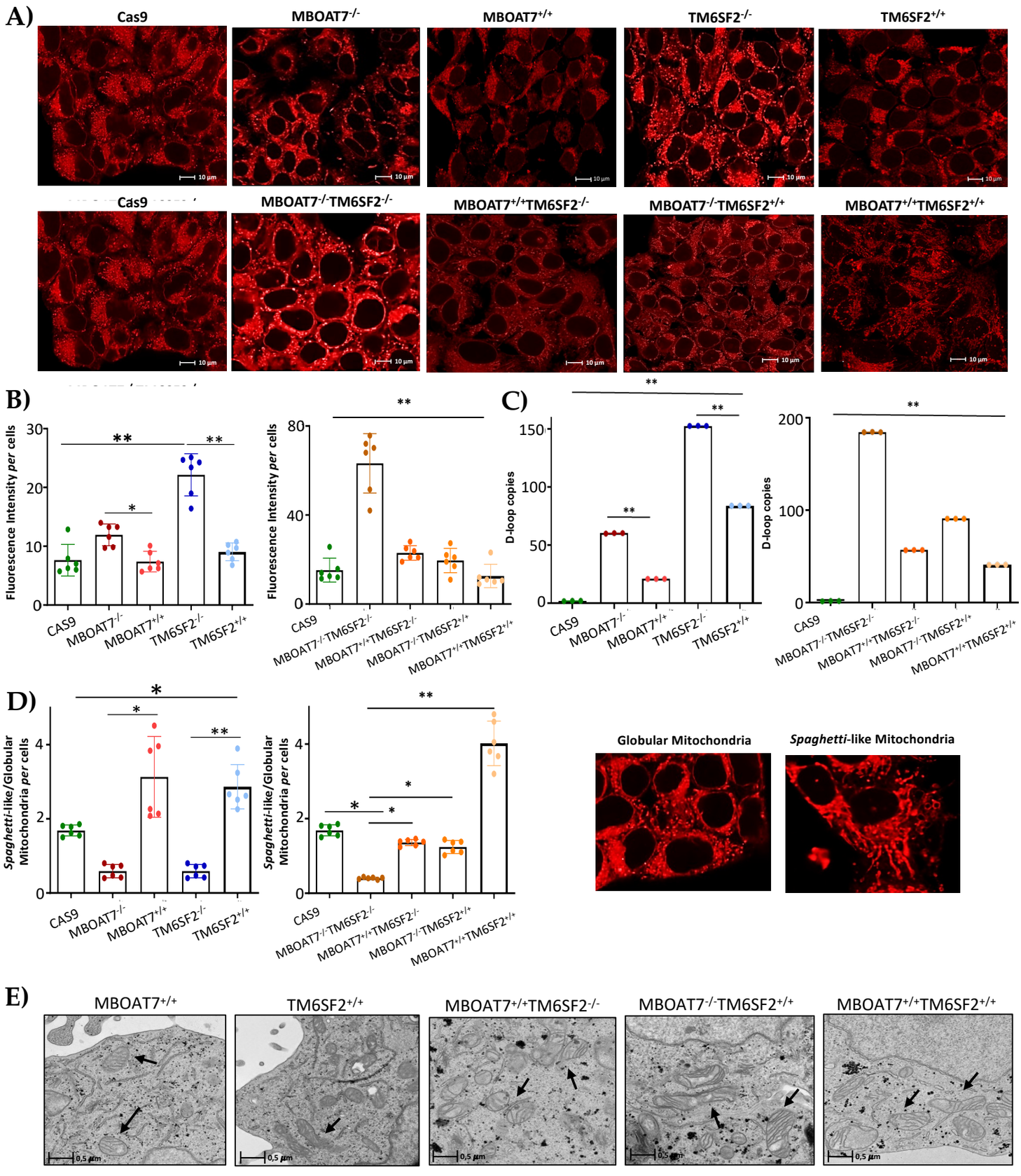
A)
Cas9
MBOAT7-/-
MBOAT7+/+
TM6SF2-/-
TM6SF2+/+
Cas9
MBOAT7-/-TM6SF2-/-
MBOAT7+/+TM6SF2-/-
MBOAT7-/-TM6SF2+/+
MBOAT7+/+TM6SF2+/+
10 µm
B)
Fluorescence Intensity per cells
CAS9
MBOAT7-/-
MBOAT7+/+
TM6SF2-/-
TM6SF2+/+
MBOAT7-/-TM6SF2-/-
MBOAT7+/+TM6SF2-/-
MBOAT7-/-TM6SF2+/+
MBOAT7+/+TM6SF2+/+
C)
D-loop copies
D)
Spaghetti-like/Globular Mitochondria per cells
Globular Mitochondria
Spaghetti-like Mitochondria
E)
MBOAT7+/+
TM6SF2+/+
MBOAT7+/+TM6SF2-/-
MBOAT7-/-TM6SF2+/+
MBOAT7+/+TM6SF2+/+
0,5 µm

Figure 3

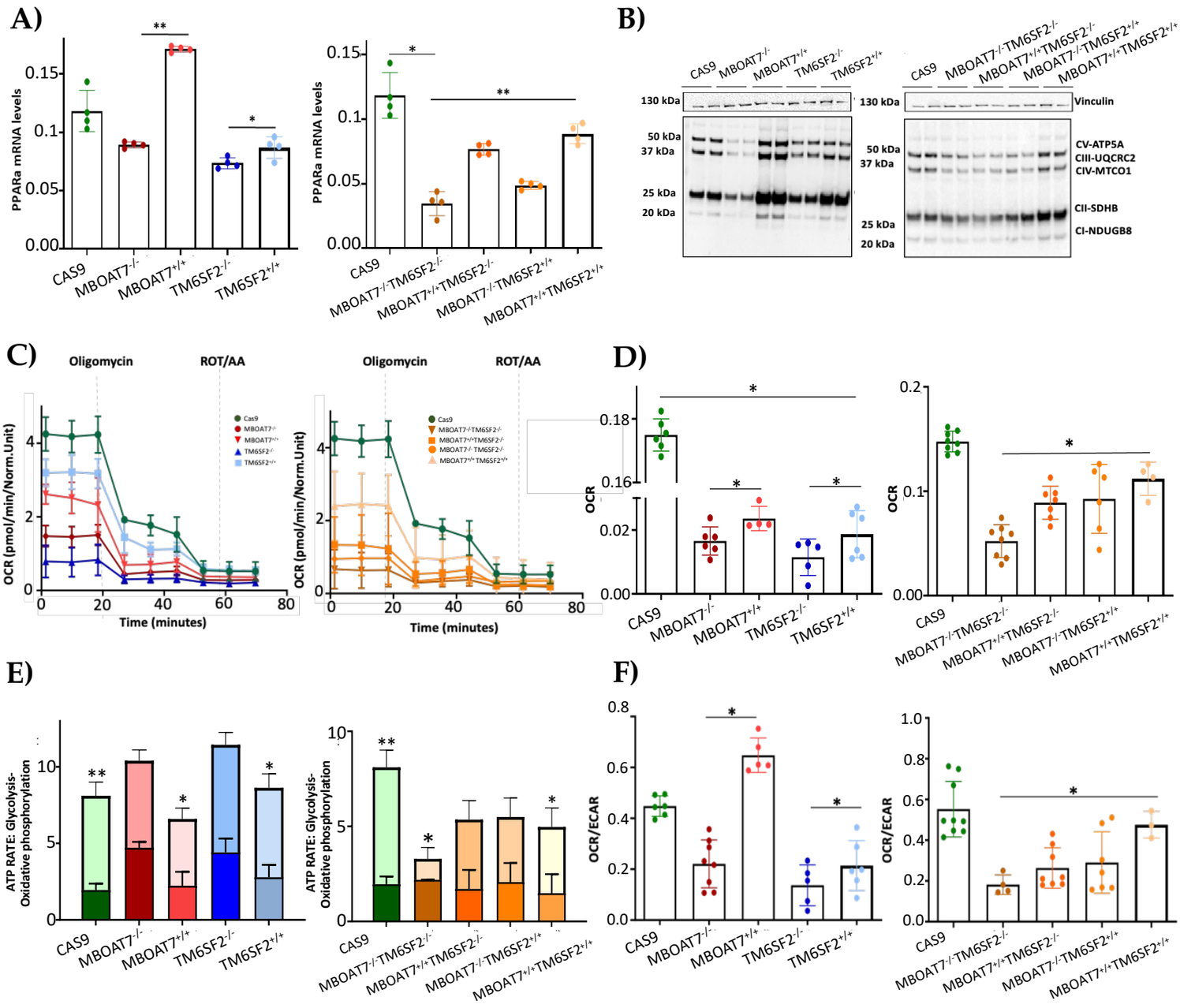
A)
PPARa mRNA levels
CAS9
MBOAT7-/-
MBOAT7+/+
TM6SF2-/-
TM6SF2+/+
MBOAT7-/-TM6SF2-/-
MBOAT7+/+TM6SF2-/-
MBOAT7-/-TM6SF2+/+
MBOAT7+/+TM6SF2+/+
B)
130 kDa
50 kDa
37 kDa
25 kDa
20 kDa
Vinculin
CV-ATP5A
CIII-UQCRC2
CIV-MTCO1
CII-SDHB
CI-NDUGB8
C)
Oligomycin
ROT/AA
OCR (pmol/min/Norm.Unit)
Time (minutes)
D)
OCR
E)
ATP RATE: Glycolysis-Oxidative phosphorylation
F)
OCR/ECAR

Figure 4

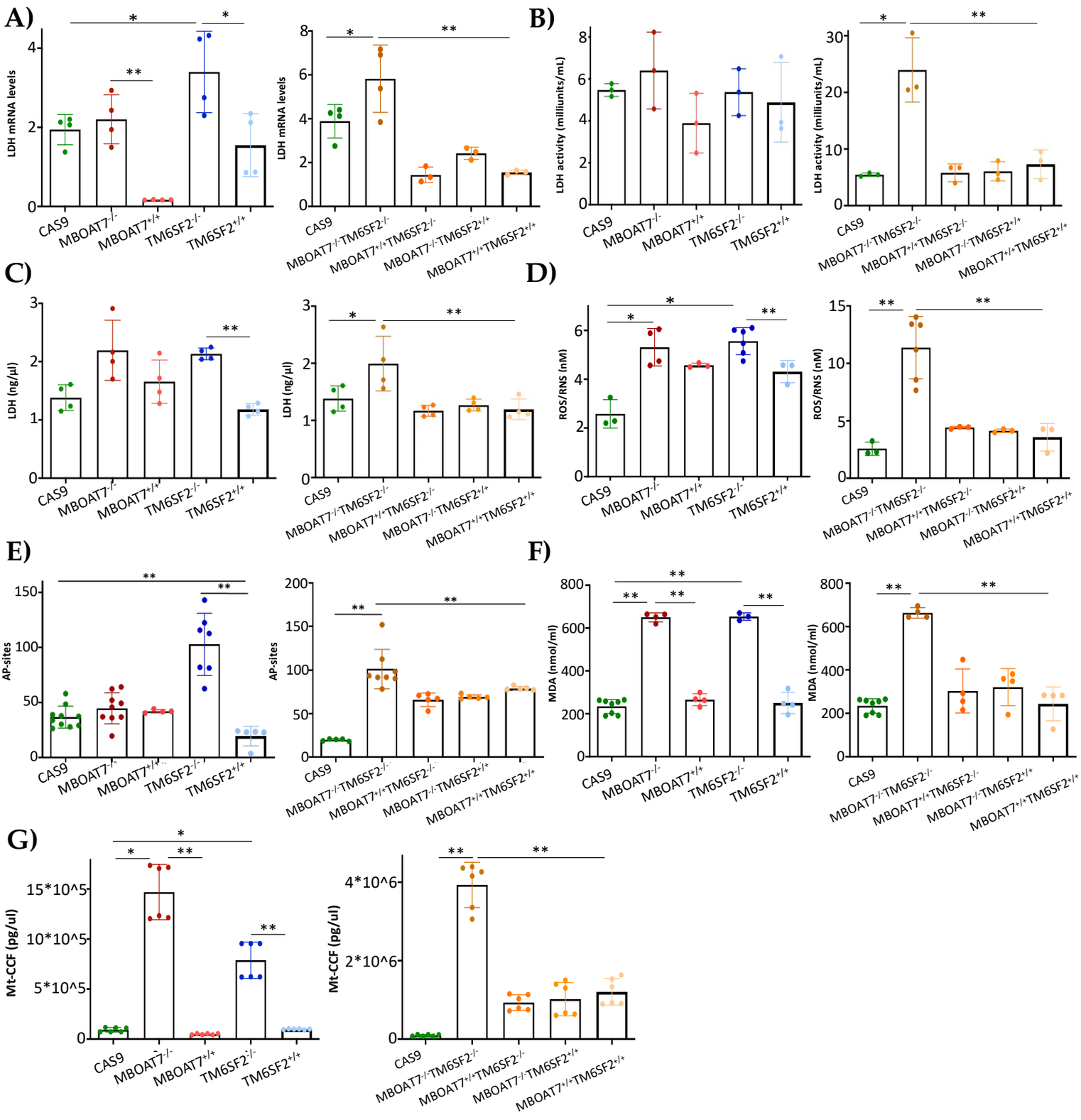
A)
B)
C)
D)
E)
F)
G)
LDH mRNA levels
LDH activity (milliunits/mL)
LDH (ng/µl)
ROS/RNS (nM)
AP-sites
MDA (nmol/ml)
Mt-CCF (pg/ul)
CAS9
MBOAT7-/-
MBOAT7+/+
TM6SF2-/-
TM6SF2+/+
MBOAT7-/-TM6SF2-/-
MBOAT7+/+TM6SF2-/-
MBOAT7-/-TM6SF2+/+
MBOAT7+/+TM6SF2+/+

Figure 5

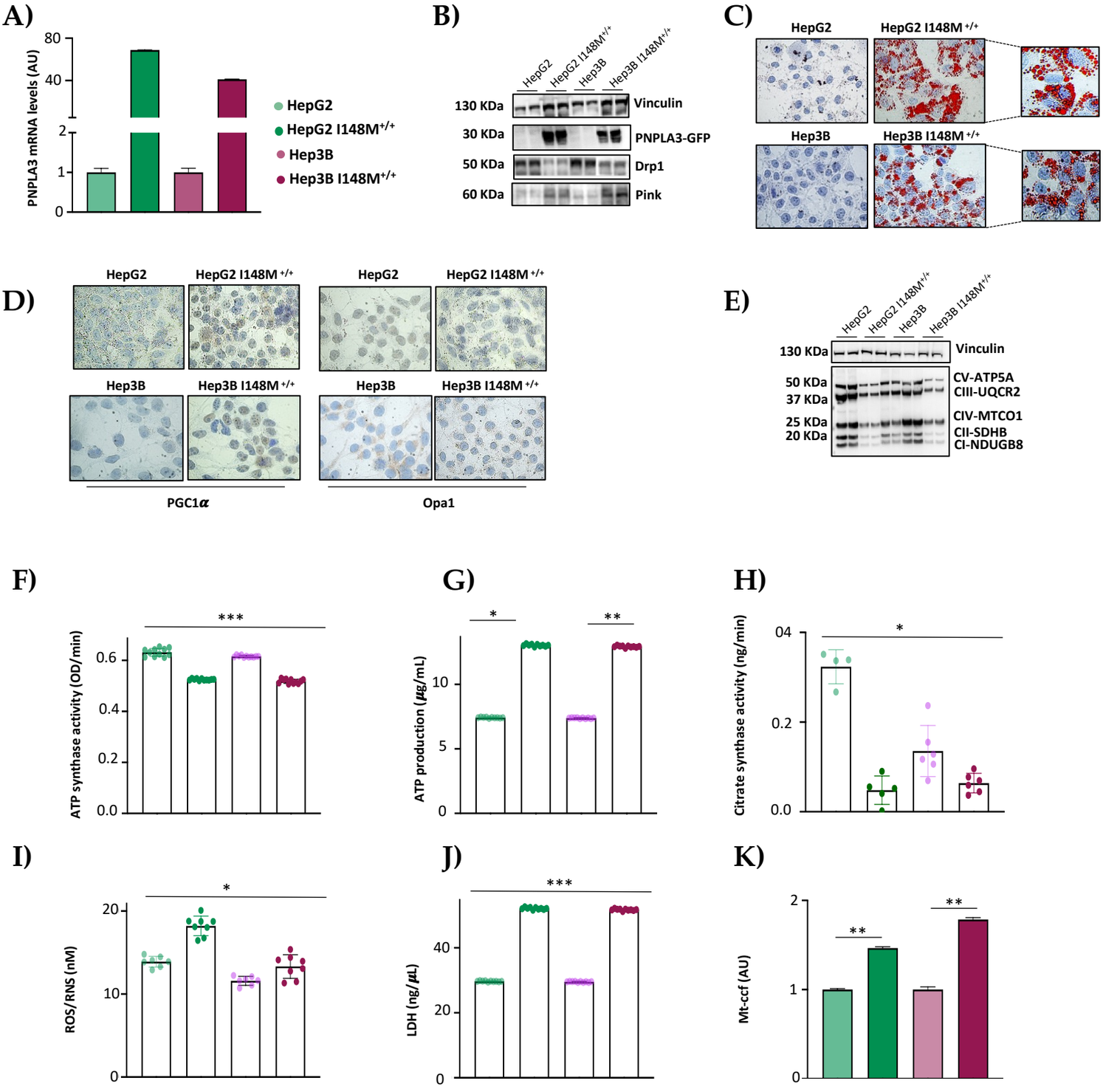
A)
PNPLA3 mRNA levels (AU)
80
40
2
1
0
HepG2
HepG2 I148M+/+
Hep3B
Hep3B I148M+/+
B)
HepG2
HepG2 I148M+/+
Hep3B
Hep3B I148M+/+
130 KDa
Vinculin
30 KDa
PNPLA3-GFP
50 KDa
Drp1
60 KDa
Pink
C)
HepG2
HepG2 I148M +/+
Hep3B
Hep3B I148M +/+
D)
HepG2
HepG2 I148M +/+
Hep3B
Hep3B I148M +/+
PGC1α
Opa1
E)
HepG2
HepG2 I148M+/+
Hep3B
Hep3B I148M+/+
130 KDa
Vinculin
50 KDa
37 KDa
CV-ATP5A
CIII-UQCR2
25 KDa
20 KDa
CIV-MTCO1
CII-SDHB
CI-NDUGB8
F)
ATP synthase activity (OD/min)
0.6
0.4
0.2
0.0
***
G)
ATP production (μg/mL)
10
5
0
*
**
H)
Citrate synthase activity (ng/min)
04
0.2
0.0
*
I)
ROS/RNS (nM)
20
10
0
*
J)
LDH (ng/μL)
40
20
0
***
K)
Mt-ccf (AU)
2
1
0
**
**

Figure 6

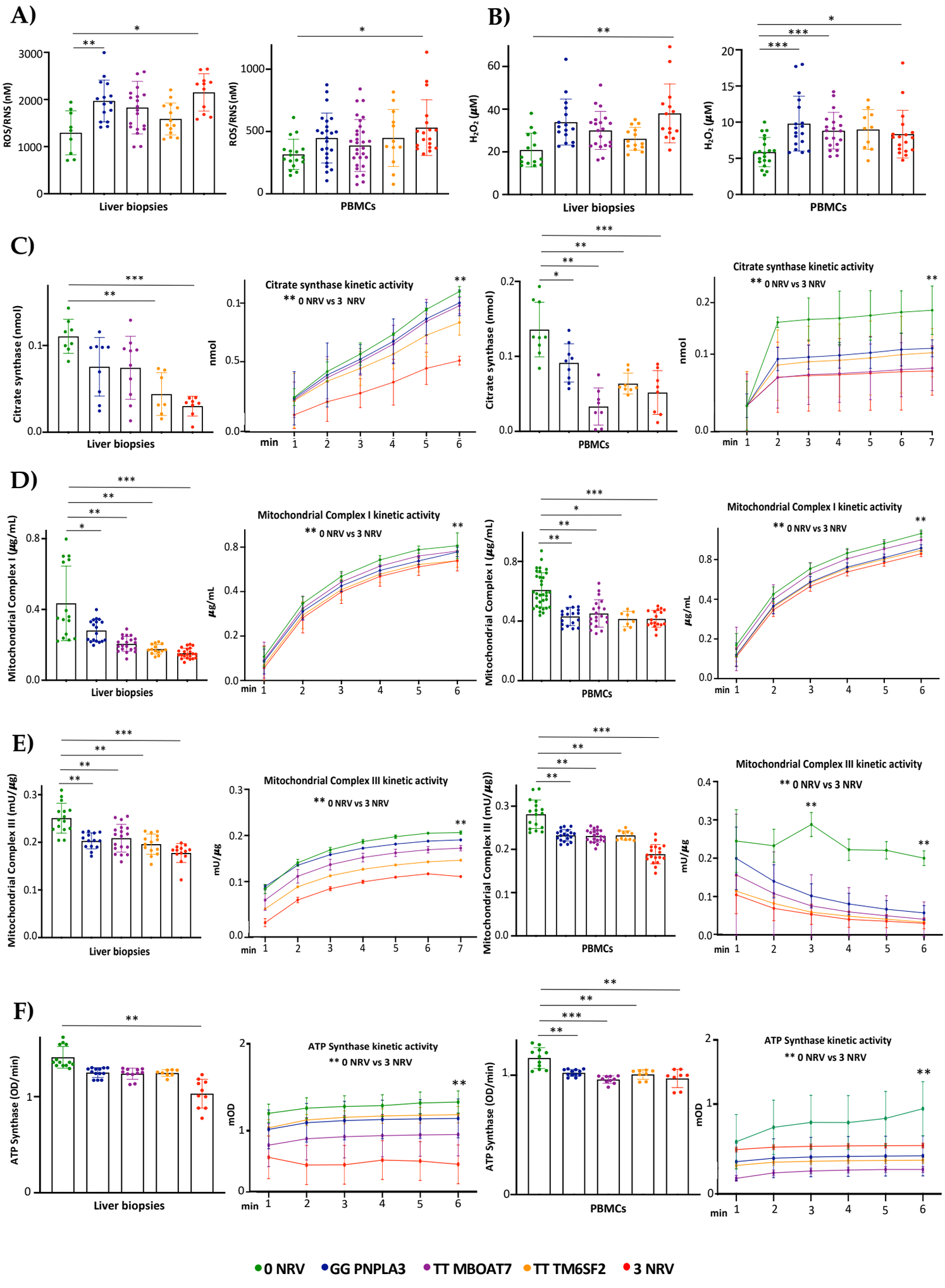
A)
ROS/RNS (nM)
Liver biopsies
PBMCs
B)
H_2O_2 (µM)
C)
Citrate synthase (nmol)
Citrate synthase kinetic activity
** 0 NRV vs 3 NRV
nmol
min
D)
Mitochondrial Complex I (µg/mL)
Mitochondrial Complex I kinetic activity
µg/mL
E)
Mitochondrial Complex III (mU/µg)
Mitochondrial Complex III kinetic activity
mU/µg
F)
ATP Synthase (OD/min)
ATP Synthase kinetic activity
mOD
0 NRV
GG PNPLA3
TT MBOAT7
TT TM6SF2
3 NRV

Figure 7

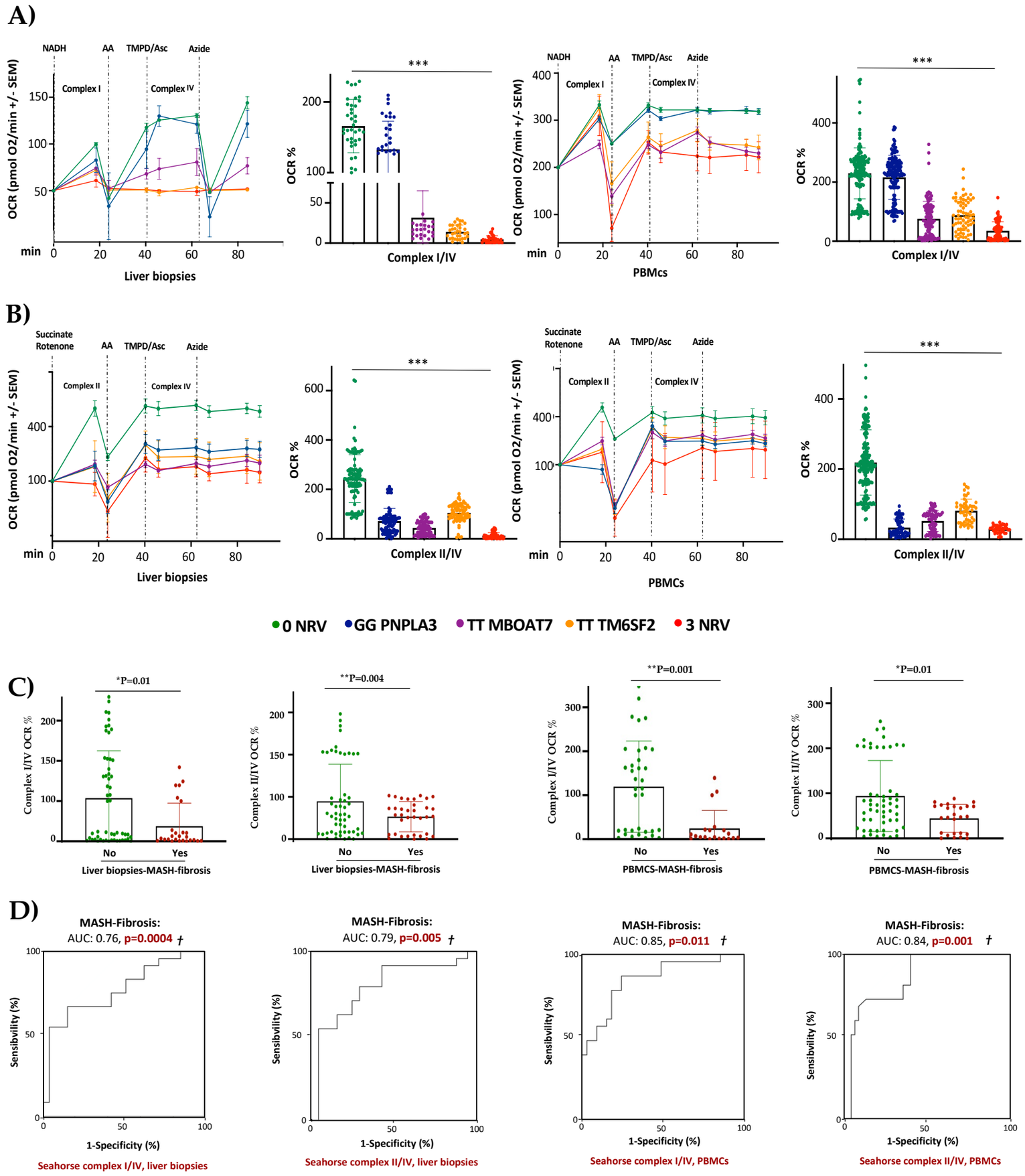
A)
NADH
AA
TMPD/Asc
Azide
Complex I
Complex IV
OCR (pmol O2/min +/- SEM)
min
Liver biopsies
OCR %
Complex I/IV
PBMCs
B)
Succinate
Rotenone
Complex II
Complex II/IV
0 NRV
GG PNPLA3
TT MBOAT7
TT TM6SF2
3 NRV
C)
*P=0.01
**P=0.004
**P=0.001
Complex I/IV OCR %
Complex II/IV OCR %
No
Yes
Liver biopsies-MASH-fibrosis
PBMCS-MASH-fibrosis
D)
MASH-Fibrosis:
AUC: 0.76, p=0.0004
AUC: 0.79, p=0.005
AUC: 0.85, p=0.011
AUC: 0.84, p=0.001
Sensibvility (%)
1-Specificity (%)
Seahorse complex I/IV, liver biopsies
Seahorse complex II/IV, liver biopsies
Seahorse complex I/IV, PBMCs
Seahorse complex II/IV, PBMCs